DYNAMICS OF MOLECULAR PHOTODISSOCIATION STUDIED USING COHERENT VACUUM ULTRAVIOLET

A Dissertation

Presented to the Faculty of the Graduate School

of Cornell University

In Partial Fulfillment of the Requirements for the Degree of

Doctor of Philosophy

by

Michael Aaron Todt

January 2017

DYNAMICS OF MOLECULAR PHOTODISSOCIATION STUDIED USING COHERENT VACUUM ULTRAVIOLET

Michael Aaron Todt, Ph. D.

Cornell University 2017

A method is described for generating intense pulsed vacuum ultraviolet (VUV) and extreme ultraviolet (XUV) laser radiation by resonance enhanced four wave mixing of commercial pulsed nanosecond lasers in laser vaporized mercury under windowless conditions. By employing noncollinear mixing of the input beams, the need of dispersive elements such as gratings for separating the VUV/XUV from the residual UV and visible beams is eliminated. A number of schemes are described, facilitating access to the 9.9 - 14.6 eV range. A simple and convenient scheme for generating wavelengths of 125 nm, 112 nm, and 104 nm (10 eV, 11 eV, and 12 eV) using two dye lasers without need for dye changes is described.

The photodissociation dynamics of OIO radicals were studied at four visible wavelengths using photofragment translational energy spectroscopy with VUV photoionization detection of the $I(^2P_{3/2})$ products. A molecular beam containing OIO was produced through the reaction IO + IO $\rightarrow$ OIO + I. Translational energy distributions of the ground state $I(^2P_{3/2})$ products indicate that O_2 is produced in both the ground $^3\Sigma_g^-$ and electronically excited $^1\Delta_g$ states. The energy change for OIO $\rightarrow$ $I(^2P_{3/2})$ + O_2 $(^3\Sigma_g^-)$ was measured to be -4.3 ± 2 kcal/mol, 1 kcal/mol more exoergic than the theoretically predicted value, but within the uncertainty of the current experiments.

The photodissociation dynamics of 1- and 2- iodopropane was studied at 266 nm using photofragment translational energy spectroscopy. Whereas 1-iodopropane dissociates exclusively to produce propyl radicals plus $I(^2P_{3/2})$ and $I(^2P_{1/2})$, HI elimination forming propene was observed from 2-iodopropane, accounting for 9% of the products. The HI is produced vibrationally excited in $v > 3$, with translational energy and angular distributions similar to the dominant $I(^2P_{3/2})$ channel. Product velocity and angular distributions were measured for all dissociation pathways using state selective photoionization as well as using electron impact ionization. Our results are compared to those from previous studies.

BIOGRAPHICAL SKETCH

Michael Aaron Todt was born in July of 1987 to Bill and Becky Todt in Orange, CA. The majority of his early life was spent in Moorhead, MN. Most of that time was spent on a bicycle, soccer field, in a swimming pool, or immersed in a book. As a child, he and his siblings often visited their father's biology laboratory classes and participated in animal dissections, sparking an early interest in science. This interest was nurtured in high school, after which he attended Augustana College (later rebranded as Augustana University) in Sioux Falls, SD to study physics and chemistry. While at Augustana, he had the opportunity to participate in three summers of undergraduate research, furthering his desire to study the intricacies of chemistry and physics. Following graduation from Augustana in 2010, he began his graduate studies in chemistry at Cornell University. Under the tutelage of Professor H. Floyd Davis, he carried out studies on the photodissociation dynamics of various iodine containing molecules as well as development of novel VUV and XUV light sources.

For my parents

ACKNOWLEDGMENTS

There are many people who have had major contributions to my academic career First and foremost is my Ph.D. advisor, H. Floyd Davis. His example as a meticulous and creative scientist has been a motivation and inspiration, allowing me to grow and learn throughout my graduate career. I will leave Cornell with a clear example of the attributes which make an efficient and effective scientist. Additionally, I would like to thank my committee members, Greg Ezra and Poul Petersen, for helpful feedback and conversations over the years.

My parents, Bill and Becky Todt, have been an unending source of encouragement and support throughout my life. Anything I have (and will ever) achieved in life is a direct reflection on their qualities as parents and role models. Also, my siblings- Kirsten, Benjamin, Annalisa, Priscilla, and Chase- have been instrumental in my life. I am truly fortunate to be surrounded by such wonderful people.

Many other people have contributed to my education as a scientist, including- but certainly not limited to- Gary Earl, Jetty Duffy-Matzner, Dwayne Weisshaar, Brain Moore, Eric Wells, Drew Alton, and Hugo Schmidt. Their enthusiasm as scientists and educators was infectious. As a complement to their educational contributions, my work at Cornell has required a strong practical and hands-on component. My time in the Graduate Student Machine Shop has been one of the most enjoyable experiences of my education, due almost entirely to the training and friendship of Nate Ellis. Also, I learned a tremendous amount from my lab-mate in the Davis group, Dan Albert. His patience and teaching ability were instrumental in my early adaptation to graduate school. As undergraduates, Neil Lawson, Adam Rettig, and Kiana Leung all spent time in the lab, and I am thankful for all of their contributions and company.

I am convinced that completing graduate school would not have been possible without the companionship and camaraderie of my classmates. In this respect, I have been

incredibly fortunate. Greg Merz was the first friend I made in Ithaca. Many late-night homework sessions and LFC games later, our contrasting personalities continue to balance each other out. Also, Greg's parents Regina and Gary have been wonderful surrogate parents to me throughout graduate school. Dan Moberg, Brain Lindley, Katie Silberstein, and Jason Lane have been tremendous companions over the years. Thanks for all the road trips, weddings, cottage weekends, and simple board game nights. Evan Ballowe and Irina Gaynanova have been huge sources of encouragement and support, for which I am forever grateful. Thanks to Doug and Donna Stauffer for bike rides, listening, and advice.

More remotely, Matt Heesch, Bryan and Bethany Kaemingk, Adam Broin, and Beth Singleton have all been great friends and confidants beginning in college and continuing through my time in graduate school. I look forward to living in closer proximity, hopefully in the near future.

Guitar and Scotch sessions with Mike Scanlon have been a highlight of every week for the past four years. Hopefully I can coordinate a trip through Ithaca on Porchfest weekend in the future so we can get the band back together. Playing soccer in the Ithaca United Soccer Club with various teams, Jorge Arriaza and the Trollers in particular, has been a pleasure and a nice excuse to get outside and run around once or twice a week.

This research was supported by the U.S. Department of Energy, under Grant No. DE-FG02-00ER15095 (Free Radical Chemistry), and by the National Science Foundation, No. CHE-1301156 (Halogen Oxide Chemistry).

TABLE OF CONTENTS

LIST OF FIGURES

LIST OF TABLES

CHAPTER 1

INTRODUCTION

I. Motivation

Photofragment translational energy spectroscopy is a powerful method for probing the dynamics of molecular dissociation upon excitation by a single photon.[1] From conservation of momentum, insight into energy partitioning into photofragments, dissociation energies, and branching between competing pathways can all be inferred. Results from these experiments are useful for testing theoretical predictions as well as providing important information necessary for accurate modeling of highly complicated systems. For example, complex models of the atmosphere require reliable data for reaction rates, dynamics, and pathways for competing reactions. In particular, reactions which have direct effects on the atmospheric ozone balance are of great interest due to their effect on the global climate.

Halogen oxide molecules have been shown to play notable roles in atmospheric chemistry, most importantly in polar ozone depletion.[2,3] The spectroscopy and photodissociation dynamics of the halogen monoxides, XO (where X = Cl, Br, I) have been studied extensively.[4,5,6,7] Larger halogen oxides, e.g. OXO, O_2X_3, etc. have also been observed in the atmosphere and have been shown to play important roles in both catalytic ozone depletion and aerosol particle formation. Cleary, understanding the branching ratios and dynamics of the competing pathways has important implications on the ozone balance in the atmosphere. Extensive studies on the chlorine oxides have been carried out over the past two decades. The photochemistry of ClO and OClO was studied first by Davis and Lee,[7,8] and subsequent studies have corroborated and elaborated on their results. However, similar studies on the triatomic bromine and iodine analogs are yet to be carried out. While

the observed concentrations of the chlorine oxides are higher than those of the bromine and iodine oxides, the reactivity of BrO has been demonstrated to be as much as 40 times greater than ClO.[9] In fact, it has been suggested that reactions involving bromine could account for as much as 40% of the ozone loss over Antarctica.[10] Clearly, studies of the reactivity and photochemistry of bromine and iodine oxides are necessary for understanding the extent of their atmospheric importance. Experimental studies of the photodissociation dynamics of OIO are presented in Chapter 3.

In Chapter 4 the photodissociation dynamics of 2-iodopropane are discussed. Simple C-I bond fission in alkyl iodides has been studied extensively, but the dissociation through four-center HI elimination has been the subject of far fewer studies. We present the first studies observing photofragment translational energy spectroscopy through this channel. Branching between the two pathways is discussed.

II. Methods

Photofragment translational energy spectroscopy experiments presented here were carried out in either the Cornell rotatable source, fixed detector apparatus (for iodine dioxide experiments, illustrated in Figure 1.1), described in detail previously[11], or in the "endstation one" rotatable source apparatus (for iodopropane experiments) originally built and housed at the Advanced Light Source at Lawrence Berkeley National Laboratory and designed to employ synchrotron undulator radiation for "soft" VUV photoionization detection of products. The apparatus, now at Cornell, has been reconfigured for photoionization detection using 8.9-11.9 eV photons generated by nonlinear conversion of tabletop nanosecond dye lasers.[12]

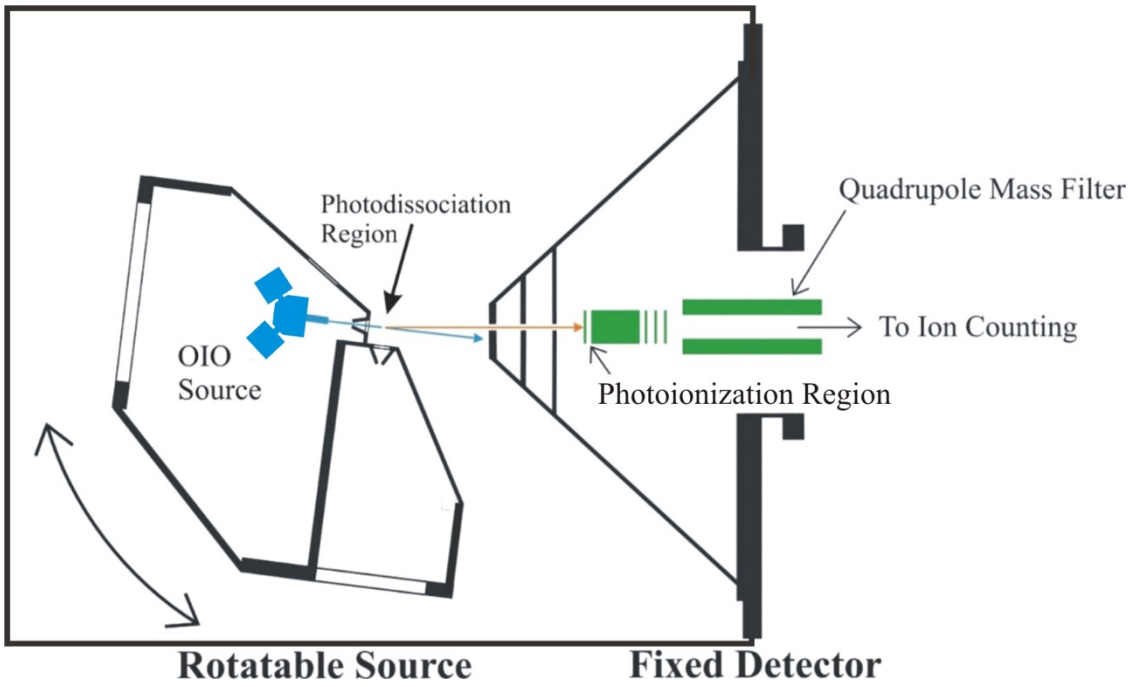

Figure 1.1 Illustration of the Cornell rotatable source chamber used for OIO photodissociation experiments.

The molecular beam in either apparatus could be rotated relative to a fixed mass spectrometer detector consisting of a photoionization region, quadrupole mass filter, and ion detector. The photodissociation laser propagates along the axis of rotation of the source assembly. A fraction of photodissociation products fly a fixed distance from the main chamber through three regions of differential pumping to the photoionization region of the UHV detector. Product time-of-flight (TOF) spectra were obtained by scanning the delay of the photoionization laser with respect to the photolysis laser using a digital delay generator (Stanford Research DG535). Detected ions for a given delay were integrated at each step using a gated photon counter (Stanford Research SR400). Signal was typically collected for several hundred laser shots at each delay step.

The photofragment lab velocity is related to the molecular beam velocity and the product Newton sphere, illustrated for OIO photodissociation at 568 nm in Figure 1.2. The

circles in Figure 1.2 represent the maximum center of mass velocities for the indicated dissociation channels. Detection at a given laboratory angle probes a slice of the Newton sphere, represented by the lines labeled in Figure 1.2. Analysis of the product TOF distributions were carried out using a forward convolution program, taking the known geometric parameters of the crossed beam apparatus, molecular beam velocity and speed ratio, source-detector angle, and user-generated product translational energy distributions, P(E), and anisotropy parameter, β, and weighting factors between competing channels as inputs. Using these parameters, the program generated TOF spectra for comparison to the experimental spectra. By iteratively adjusting the relative weight and distributions of the input P(E)s, the theoretical TOF was adjusted to match experimental data. Through conservation of energy, the internal energy of the parent molecule (e.g. OIO) and photon energy is related to the translational and internal energy of the photofragments ($I + O_2$):

$$E_{photon} + E_{int,OIO} = D_0(OIO \rightarrow I+O_2) + E_{trans,I+O2} + E_{int,I} + E_{int,02}$$

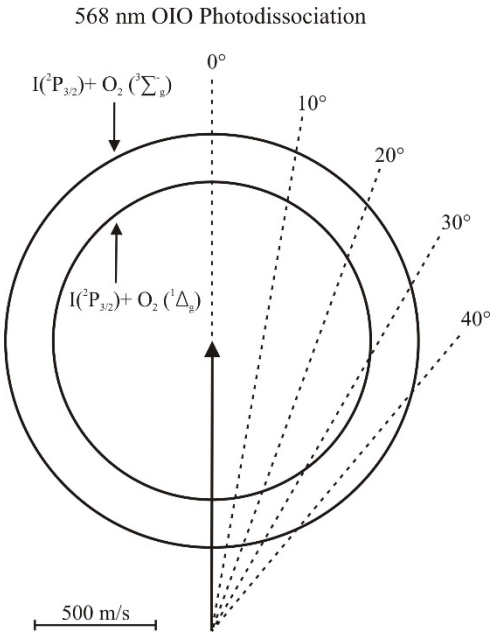

Figure 1.2: Newton diagram in velocity space for photodissociation of OIO at 568 nm. The circles represent the maximum velocities of $I(^2P_{3/2})$ with the counterfragment O_2 in v = 0 of the indicated electronic states.

Efficient detection of photofragments is of paramount importance for photofragment translational energy spectroscopy. Over the years, many detection methods have been used. Perhaps the most straightforward detection method is through electron impact ionization, followed by ion detection using standard quadrupole mass spectroscopy techniques. The major advantage of electron impact ionization is universality of the ionization method. Electrons with high (15-100 eV) energy are capable of ionizing essentially any molecule, making this method useful for detection of a variety of products with minimal changes to the experimental setup. Downsides to electron impact ionization include small ionization cross sections and a high degree of molecular fragmentation.

Using single-photon soft ionization with vacuum ultraviolet (VUV) radiation allows for nearly universal ionization of molecules. If the photon energy is above the ionization energy of the molecule of interest, ionization probabilities for molecules tend to be much higher for single photon ionization than for electron impact ionization. Generation of VUV is relatively straightforward, and has been used to great effect for decades.[13,14,15] Typical VUV generation techniques depend on four-wave sum-frequency mixing in high pressure mixing region. This is not a problem when the generated VUV can be efficiently transmitted through a window or lens separating the mixing and detection regions. However, since no solids are capable of transmitting wavelengths shorter than 104 nm (the LiF cutoff wavelength), windowless configurations must be used.

In Chapter 2, a novel method for production of VUV and extreme ultraviolet (XUV) radiation is described which facilitates *windowless* operation, bypassing the need for optics by generating VUV and XUV in a low pressure region. The generated radiation is spatially separated from the input radiation via noncollinear mixing in laser vaporized Hg, to

maintain low mixing region pressure. In Chapter 4, a second windowless method is used which involves four-wave mixing in long heated Hg cell using unfocused lasers, as described by this lab previously[16], but after generation of VUV radiation, the lasers pass through a long, thin tube (I.D. 3mm, 45 cm long) which restricts the conductance of gas used in the Hg cell. Two stages of differential pumping are sufficient to maintain adequately low pressures for windowless operation.

In Chapter 4, single photon VUV ionization is used to detect I*($^2P_{1/2}$), propyl radical, and HI products from photodissociation of 1- and 2-iodopropane. However, depending on the information desired, universal detection of products may not be desirable. For *state specific* detection of molecules, resonance enhanced multi photon ionization (REMPI) is a powerful technique. In REMPI schemes, the molecule of interest is excited from a lower energy quantum state to a higher energy quantum state via a one or two photon transition as specific wavelength. For the studies presented here, (1+1) REMPI detection is used to probe ground state I($^2P_{3/2}$) photofragments. The VUV photon energies are insufficient for single photon ionization of I, thus ionization is dependent upon a second visible photon imparting sufficient energy for ionization. By selectively detecting ground state I atoms, it is known that all available energy imparted by the photodissociation laser can be distributed only to translational energy of photofragments or into internal excitation of the counterfragment.

III. References

1 . P. Ho, D.J. Bamford, R.J. Buss, Y.T. Lee, and C.B. Moore, *J. Phys. Chem.*, **76**, 3630 (1982).

2. M.B. McElroy, R.J. Salawitch, S.C. Wofsy, and J.A. Logan, *Nature* **321**, 795 (1986).

3. R.P. Wayne, G. Poulet, P. Biggs, J.P. Burrows, R.A. Cox., P.J. Crutzen, G.D. Hayman, M.E. Jenkin, G. LeBras, G.K. Moortgat, U. Platt and R. N. Schindler, *Atmos. Envir*. **29**, 2677 (1995).

4. K.A. Peterson, B.C. Shepler, D. Figgen, and H. Stoll, *J. Phys. Chem. A.* **110**, 13877 (2006).

5. P. Zou, H. Kim, and S.W. North, *J. Chem. Phys*. **116**, 4176 (2002).

6. K.S. Dooley, J. N. Geidosch, S.W. North, *Chem. Phys. Lett.*, **457**, 303 (2008).

7. H.F. Davis and Y.T. Lee, *J. Phys. Chem.* **100**, 30 (1996).

8. H.F. Davis and Y.T. Lee, *J. Chem. Phys.* **105**, 8142 (1996).

9. J. S. Daniel, S. Solomon, R. W. Portmann, and R. R. Garcia, *J. Geophys. Res.* **104**, 23871 (1999).

10. R. Schofield, P. V. Johnston, A. Thomas, K. Kreher, B. J. Connor, S. Wood, D. Shooter, M. P. Chipperfield, A. Richter, R. von Glasow, and C. D. Rodgers, *J. Geophys. Res.* **111**, D22310 (2006).

11. P.A. Willis, H.U. Stauffer, R.Z. Hinrichs, and H.F. Davis, *Rev. Sci. Instrum.* **70**, 2606 (1999).

12. "Synchrotron Radiation Techniques in Industrial, Chemical, and Materials Science", ed. Kevin L. D'Amico, Louis J. Terminello, David K. Shuh, 1996

13. J.W. Hepburn, “Applications of Coherent Vacuum Ultraviolet to Photofragment and Photoionization Spectroscopy,” in *Vacuum Ultraviolet Photoionization and Photodissociation of Molecules and Clusters*, C.Y. Ng, ed. (World Scientific, Singapore, 1991) pp. 435-485.

14. R. Hilbig and R. Wallenstein, *Appl. Opt.* **21**, 913 (1982).

15. K.S.E. Eikema and W. Ubachs in *Handbook of High Resolution Spectroscopy*, edited by M. Quack and F. Merkt (John Wiley & Sons, 2010) pp. 1374-1413.

16. D R. Albert, D.L. Proctor, and H.F. Davis, *Rev. Sci. Instrum.* **84**, 063104 (2013).

CHAPTER 2

HIGH INTENSITY VUV AND XUV PRODUCTION BY NONCOLLINEAR MIXING IN LASER VAPORIZED MEDIA

I. Introduction

Four-wave sum frequency mixing of commercial tunable nanosecond pulsed lasers in gases is a well-established method for producing coherent vacuum ultraviolet (VUV, $\lambda < 180$ nm) and extreme ultraviolet (XUV, $\lambda < 110$ nm) radiation.[1,2,3] A thorough summary of current XUV and VUV generation methods and uses, written by Eikema and Ubachs, can be found in the *Handbook of High Resolution Spectroscopy*.[4] These wavelengths span photon energies where gaseous molecules undergo photodissociation and/or photoionization. Many schemes employing inert gases (particularly Kr and Xe) have been reported, with the greatest efficiencies obtained by exploiting the large resonance enhancements in $\chi^{(3)}$ in the vicinities of one- and two-photon resonances.[5] In certain wavelength regions, conversion efficiencies can be further improved by optimal phase matching using gas mixtures.[5,6,7] By employing resonance enhancement and phasematching simultaneously, conversion efficiencies approaching 0.1% can be achieved under favorable conditions in Kr or Xe.[5,7]

The extremely large nonlinear susceptibilities of metallic gases such as mercury (Hg) lead to conversion efficiencies into the VUV/XUV that can be orders of magnitude greater than for inert gases.[1,8,9,10] For example, by tuning a single frequency-doubled dye laser to the $6\,^1S_0$-$7\,^1S_0$ two-photon resonance in Hg at 312.85 nm, and mixing in the residual 625.70 nm fundamental, ~10^{13} photons/pulse near 10 eV can be produced in a focused configuration using heated cell.[9,10] This corresponds to conversion efficiencies from the

UV greater than 1%.[9,10] We recently described schemes for mixing of two or three collimated (unfocused) beams from commercial dye lasers in 1 m long Hg heat pipes for production of ~0.1 mJ pulses (6 x 10^{13} photons/pulse) near 125 nm and 130 nm.[11] Because the laser beams are unfocused, by scaling the input laser beams to higher energies, VUV output pulse energies in the millijoule range are achievable.[12,13] In this wavelength range, MgF_2 and LiF optics can be employed for focusing or dispersing the VUV from the much more intense UV and visible beams with modest power losses, *e.g.*, by transmission through a lens held off of the optical axis.[11,13,14]

The optical transmission of window materials decreases sharply at shorter wavelengths, falling to zero for LiF at $\lambda < 104$ nm.[15] For MgF_2, the only other material capable of transmitting light at $\lambda < 140$ nm, the transmission cutoff occurs at 116 nm.[15] Consequently, a number of windowless schemes have been developed for operation in the XUV.[16,17,18,19] One approach employs a capillary array to transmit XUV light from the high pressure region (where 4-wave mixing is carried out) to a lower-pressure region such as the ionization source of a mass spectrometer.[16,19,20] For mixing in inert gases, a simple approach involves nonlinear conversion in pulsed gas jets.[21,22,23,24,25] Due to the very small gas load, the XUV can be propagated through a single differentially pumped aperture, thereby avoiding the need for window material or capillary arrays.

Many scientific applications require separation of the XUV from the much more intense residual UV and visible laser beams, usually requiring dispersion by a grating.[24,25] This approach is expensive, particularly because gratings are susceptible to optical damage by high-power laser beams. From a practical perspective, the efficiencies of gratings are typically only ~10%, severely limiting the usable XUV photon flux.

Clearly, four-wave mixing of commercial nanosecond lasers facilitates access to the VUV region with efficiencies sufficient for many scientific applications. Unfortunately, due to the need for windowless operation and the low efficiency of dispersive elements such as gratings, efficient access to the XUV region by nonlinear conversion of tabletop laser systems has remained quite challenging from an experimental perspective. In the present work, we sought an experimental approach that would increase conversion efficiencies while simultaneously simplifying the experimental setup by eliminating the need for capillary arrays, extensive differential pumping, and optical elements such as gratings.

If the two input laser beams are crossed at a small angle, four wave mixing produces an output beam that propagates in a direction different from the residual input beams. This eliminates the need for dispersive elements such as gratings for wavelength separation.[4,26,27] To date, this approach has been carried out using inert gases (e.g., Xe) in static cells[26] or in pulsed jets[27] as the nonlinear medium. Peet and Tsubin compared the efficiencies for resonance-enhanced third harmonic generation in Xe using both collinear (single beam) and noncollinear (two crossed sub-beams) and found that both modes provide nearly the same conversion efficiencies but with different tuning curves.[26] It should be noted that noncollinear schemes have also been demonstrated theoretically and experimentally with femtosecond laser systems, by nonresonant four wave mixing, in a transparent solid, e.g. LiF, CaF_2 or fused silica.[28,29,30,31] In these cases, the intersection angle of the input beams were chosen to optimize phase-matching conditions for four wave mixing. In our experiments, the input wavelength is scanned to optimize phase-matching for a given crossing angle.

The use of a continuous Hg gas jet for VUV generation has been reported.[32] However, this approach is complex and is could present a safety hazard due to the need for vaporizing and recycling large volumes of liquid Hg. Chénais and coworkers generated VUV in a Hg plume produced by laser vaporization from liquid Hg in a room temperature cell.[33] The use of laser vaporization of Hg is extremely attractive because very small Hg samples can be employed and no active pumping is needed to recirculate the Hg. Furthermore, because the vapor pressure of Hg is $2x10^{-3}$ Torr at room temperature[34], a single stage of differential pumping makes windowless operation straightforward.

In the work reported by Chénais, only a single dye laser was available for generating the input beams, i.e., 625.70 nm and 312.85 nm, corresponding to the fundamental and second harmonic of a DCM dye laser.[33] Therefore, the generated output beam (near 125 nm) was not tunable, and no attempt was made to separate the VUV from the residual input beams. They reported pulse energies up to 5 μJ ($3x10^{12}$ photons/pulse), which were comparable to values reported using heated cells.[33] We note that near 125 nm, the well-established heated cell method[9] with LiF or MgF_2 optics is simple and reliable. Therefore, the added complexity of a laser vaporization source (requiring an independently triggered Nd:YAG or excimer laser for vaporization) is probably not justified. However, for production of radiation at shorter wavelengths, especially where transmission through LiF or MgF_2 windows becomes inefficient or zero, the benefits of laser vaporization justify the added complexity.

Several articles have appeared reporting production of high VUV intensities (10^{13} photons/pulse) by four wave mixing in *room temperature Hg in the absence of laser vaporization.*[35,36] While we were able to produce VUV using room temperature ambient Hg, the intensities were at least two orders of magnitude smaller than using heated Hg cells or the laser vaporization method described here.

Difference frequency mixing ($2\omega_1 - \omega_3 = \omega_{VUV}$) in inert gases facilitates production of broadly tunable VUV.[7] Sum frequency mixing schemes ($2\omega_1 + \omega_3 = \omega_{VUV}$) producing broadly tunable XUV have also been described.[23,24,25] However, for many applications, broad tunability is not necessary, and instead the highest conversion efficiencies into the VUV or XUV are desirable at a single wavelength or over a limited wavelength range. For production of VUV at photon energies below the Hg ionization limit (10.43 eV), the efficiencies for VUV production vary strongly with wavelength.[9,10] However, at higher energies the XUV is continuously tunable.[19,20]

We have employed noncollinear mixing of input laser beams in laser vaporized Hg to produce VUV and XUV wavelengths ranging from $\lambda = 125$ nm (9.9 eV) to $\lambda = 96.9$ nm (12.8 eV) utilizing the $6\ ^1S_0$-$7\ ^1S_0$ two photon resonance in Hg (Fig. 2.1). Comparisons are made between this method and the use of a standard heated cell configuration,[9] both in collinear and noncollinear geometries. Absolute VUV intensity measurements at 125 nm, 121 nm, 112 nm, 104 nm, and 96.9 nm are provided. Tuning curves through the $9\ ^1P_1$ and $12\ ^1P_1$ resonances in Hg are also provided for both collinear and noncollinear geometries. In addition, a number of wavelengths utilizing higher energy two photon resonances have also been explored, leading to higher energy photons (up to 14.6 eV) at lower intensities.

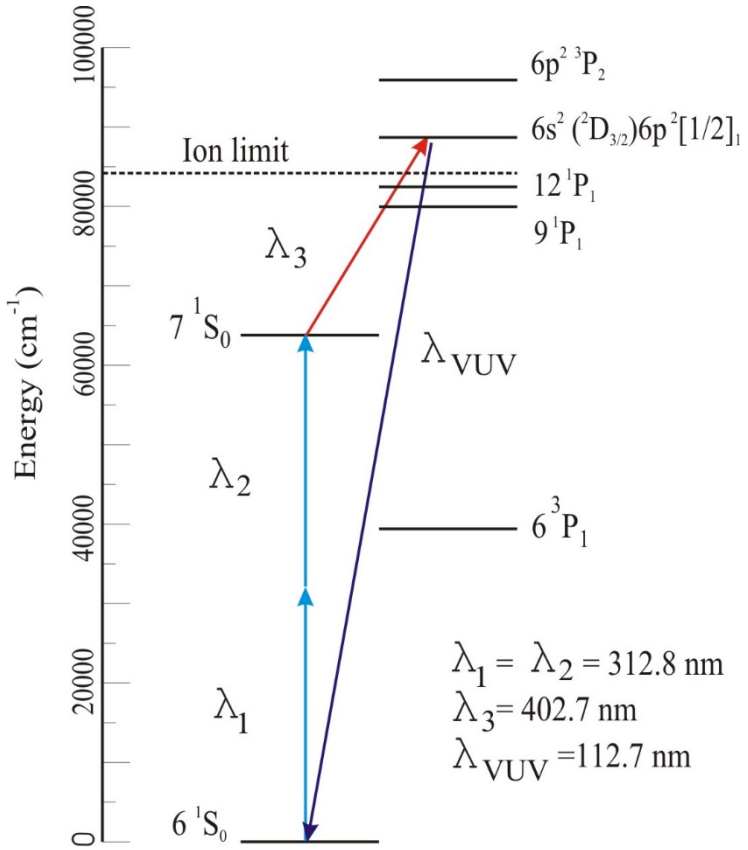

Figure 2.1: Partial energy level diagram for Hg. Production of 112.7 nm light (11.0 eV) is illustrated.

II. Experimental

The 312.85 nm light tuned to the 6 $^1S_0$-7 $^1S_0$ two-photon transition in Hg was generated by frequency-doubling the output of a Nd:YAG pumped (Continuum Powerlite 8010, 532 nm, 8 ns/pulse, 10 Hz) tunable dye laser (either Lambda-Physik Scanmate 2 or FL3002) using DCM dye tuned to 625.7 nm. Visible and UV light was produced using a second tunable dye laser (Scanmate 2), pumped by either the 532 nm or 355 nm output from the same Nd:YAG laser. In the cases where $\lambda_3 < 400$ nm, the output of the second dye laser was frequency-doubled. Sum frequency mixing involved $\omega_{VUV} = 2\,\omega_1 + \omega_2$, with ω_{VUV} tunable by tuning ω_2. Table 1 summarizes pertinent information concerning the three input wavelengths (λ_1, λ_2, and λ_3) and the resulting λ_{VUV}.

Table 2.1: Summary of wavelengths used for VUV generation, pulse energy, VUV photon energy, dye used, and maximum number of photons produced per pulse.

λ_1 (nm)	Pulse energy (mJ)	λ_2 (nm)	λ_3 (nm)	Pulse energy (mJ)	λ_{VUV} (nm)	Photon Energy (eV)	λ_3 Laser Dye	VUV Photons/ pulse
313	5.5	313	625	7.0	125	9.9	DCM	$5x10^{12}$
313	2.5	313	540	4.0	121	10.2	C540A[1]	$2x10^{11}$
313	3.0	313	403	5.5	112	11.0	Ex 404[2]	$2x10^{11}$
254	0.8	408	408	4.5	112	11.0	Ex 404[2]	$5x10^{11}$
313	2.5	313	312	2.5	104	11.9	DCM[3]	$9x10^{10}$
254	0.8	254	408	4.5	97	12.8	Ex 404[2]	$2x10^{8}$
269	1.0	269	269	1.0	90	13.8	C540A[1,3]	$3x10^{7}$
255	0.7	255	255	0.7	85	14.6	LDS 765[4]	$6x10^{6}$

The experimental setup is illustrated in Fig. 2.2. The two input laser beams (~2 mm diameter) were initially focused through the center of a 34 cm focal length achromatic lens (Optics for Research) and aligned through the Hg cell and interaction regions collinearly to produce maximum VUV intensities. The final mirrors for each input beam were mounted on separate translation stages. This made it possible to independently translate each beam away from the center of the lens, with one beam at the 3 o'clock and the other at the 9 o'clock positions on the lens. When in a non-collinear geometry, the VUV beam

[1] Coumarin 540A laser dye
[2] Exalite 404 laser dye
[3] Frequency doubled
[4] Frequency tripled

propagated at an angle between the two initial beams, determined by the input photon energies and crossing angle. In this case of $\lambda_1 = \lambda_2$, if the propagation of λ_1 laser is defined as $\theta=0$, then $\theta_{VUV} = \theta_{crossing}[\omega_3/(2\omega_1 + \omega_3)]$.

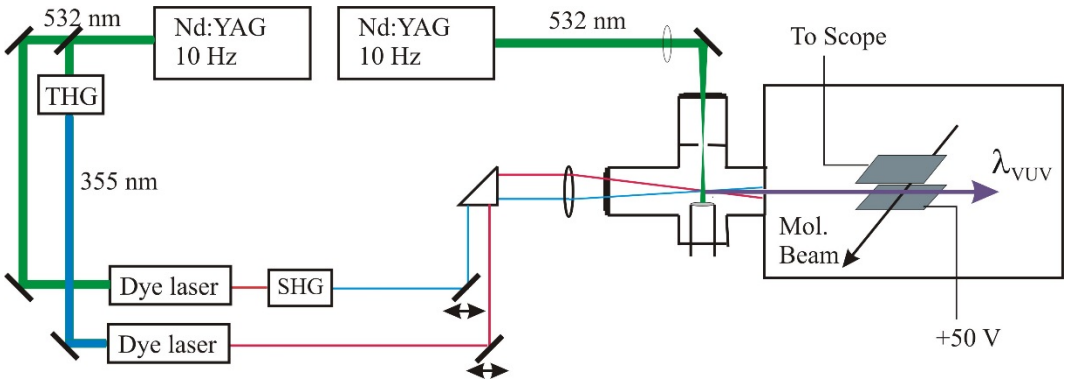

Figure 2.2: Laser table layout. Output of each of the two dye lasers is temporally and spatially overlapped, with translation stages for each beam before being focused into the Hg cell. The detection method shown is the 2-plate detector.

Figure 2.3 shows a more detailed view of the ablation cell. The ablation cell was built using a 2.75" six-way conflat cross (MDC) with input and output arms each extended by 5" using stock 2.75" conflat nipples (MDC). The Hg reservoir is a 1'' diameter stainless steel rod with a 3/4'' diameter, 1/8'' deep counterbore to contain the Hg. Water channels (0.25" dia.) were drilled through the length of the rod to allow cold water from a thermostatically-controlled refrigerated bath (Neslab RTE-111) to be circulated, thereby cooling the mercury sample to ~7°C. The vapor pressure of Hg at this temperature is ~4.1 x 10^{-4} Torr.[34] The 6-way cross was evacuated continuously by a small vacuum pump connected via a needle valve. Even after many months of operation, the amount of Hg removed by the vacuum pump was negligible. The 1" diameter rod was sealed to the bottom of the 6-way cross using a Cajon fitting with o-ring seal, making it possible to translate the

entire rod up and down to precisely locate the surface of the mercury pool relative to the laser axis. The laser input window was heated to ~30^{o}C (by wrapping the arm with heating tape) to prevent Hg buildup. The ablation source and detection chamber were separated by a double-sided 2 3/4'' conflat flange with a 1 mm diameter centrally-located hole. The entire Hg cell assembly was sealed to the vacuum chamber via a 2.75" gate valve (MDC). The valve was kept closed except during experiments.

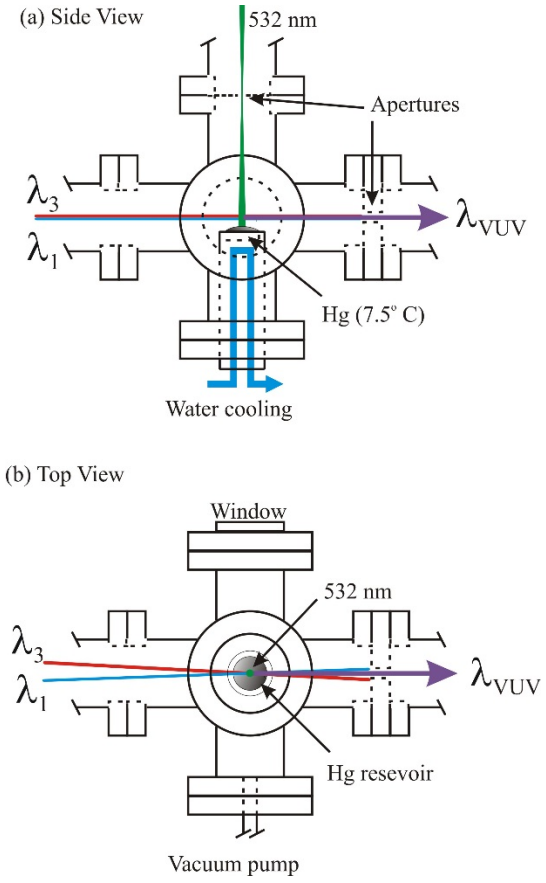

Figure 2.3: Schematic of the ablation mixing cell. (a) side view and (b) top view.

The degree of spatial separation of λ_{VUV} from λ_3 and λ_1 is directly related to the angle between the input beams introduced by walking the beams away the central axis of the focusing lens. For a given crossing angle, as λ_3 decreases, the separation between the λ_1 and λ_{VUV} beams increases. For example, using 312.85 nm and 625 nm input beams, in order to separate the centers of the VUV and 312.85 nm beam by a beam diameter (~2 mm) at the photoionization region located 35 cm from the lens, the 312.85 nm and 625 nm beams must be translated 2 and 8 mm from the center of the lens, respectively. However, for mixing 312.85 nm and 312 nm beams, the beams needed only to be translated 2 and 4 mm, respectively, from the center of the lens to produce the same separation between the 312.85 nm and VUV beams. In practice, the angles employed in this work were chosen in order to minimize background from 104 nm radiation (discussed below) while being limited by the physical dimensions of the achromatic lens. The optimal interaction angle for a given setup will depend on the wavelengths of the input lasers, VUV wavelength, and physical limitations of the experimental apparatus.

The VUV beam direction will change slightly as λ_3 is scanned. Across the tuning range of a typical laser dye for λ_3, the change in VUV photon energy is less than 3%, leading to small changes in VUV pointing direction. For example, scanning λ_3 from 610 nm to 660 nm, the angle through which the VUV beam moves is 0.02^o (0.13 mm when measured 35 cm from the focal point). The effect of this small change in VUV pointing direction was not significant in our experiments. If the VUV propagation distance is significantly longer, the wavelength dependence of the VUV propagation angle could become important.

The VUV beam intensities were monitored by photoionization of various gases with well-established ionization energies (I.E.) and photoionization cross sections.[37] The propene (I.E. = 9.7 eV), acetylene (I.E. = 11.4 eV), and 1-butene (I.E. = 9.6 eV) beams were produced by a piezoelectrically-operated pulsed valve. Photo ions were detected using either a Wiley-McLaren time-of-flight mass spectrometer or by collection using two stainless steel plates, one held at + 50V and the other connected to a digital oscilloscope (terminated 50Ω to ground) where the signal was read as a time dependent voltage. Absolute VUV intensities were calculated using the density of the molecular beam, photoionization cross section, and oscilloscope signal with the voltage integrated over the pulse width. The detection efficiency was calibrated in a separate series of experiments at 125 nm using a slow flow of a gas into the chamber at measured total pressure. After the absolute VUV intensity had been calculated at 125 nm it was possible to use the absolute signal level at a given mass in the TOF spectrum to compare between different schemes under the same TOF conditions, i.e. the same microchannel plate voltage, ion optics setting, and molecular beam conditions. The different photoionization cross sections were used to compare VUV and XUV intensities at different wavelengths. [37,38] For schemes producing high VUV intensities, the TOF peaks were sometimes distorted due to space charge effects, making intensity measurements impossible. In these cases, we either used the two-plate detection method using the same molecular beam, or decreased the concentration of gas in the molecular beam.

Absolute measurements of VUV and XUV intensities are difficult. We estimate the uncertainty in absolute VUV intensity at 125 nm to be ±50%. The VUV and XUV intensities reported at 121 nm, 112 nm, and 104 nm have been calculated based on signal

levels relative to that at 125 nm. These measurements are subject to the same systematic error as the 125 nm VUV, with a further ±10% uncertainty for each of these measurements (±55% overall). Intensities for shorter wavelengths have been calculated in a similar manner relative to 104 nm intensity, inducing a further ±10% uncertainty (±60% overall).

The 532 nm output of a second Nd:YAG laser (Continuum NY 81-10 or Surelite II) was used for Hg vaporization. A half wave plate and polarizer were used to adjust the pulse energy without affecting the spatial beam profile. The laser was focused 8 cm above the Hg surface using a 40 cm focal length lens, producing a spot diameter of approximately 2 mm on the Hg surface. In order to prevent Hg vapor from reaching the ablation laser input window, the ablation laser was focused through a plate with a 2 mm hole drilled through it, located at the focal point of the laser. Figure 2.3 shows the configuration of the ablation cell. The timing and alignment of the ablation laser was critical for optimal VUV generation; the Hg density in the mixing region is affected by both the ablation laser pulse energy and the delay time between the ablation laser and the UV and visible lasers. The optimal delay was varied using an SRS DG535 digital delay generator. Typically, the ablation laser was triggered 5-20 μs before the UV and visible dye lasers. When the 312.85 nm laser was well overlapped both spatially and temporally with the Hg plume, bright blue fluorescence was visible at the 312.85 nm focus. This fluorescence was most likely due to fluorescence from $7^1S_0 \rightarrow 6^3P_1$ at 407.8 nm,[39] and was not visible if the 312.85 nm laser wavelength was detuned or the timing between the dye lasers and the ablation laser was not optimal. The presence of the blue fluorescence was a useful visible check for correct alignment, wavelength, and timing.

A simple and versatile configuration facilitates convenient access to photon energies of 9.9 eV, 11.0 eV, and 11.9 eV without the need for any dye changes. One DCM dye laser was used to produce light at λ = 312.85 nm. The second DCM laser generated 625 nm radiation to produce 9.9 eV photons. To obtain 11.0 eV photons, 650 nm radiation (produced using the same DCM dye) was mixed with the 1064 nm output of the unseeded Nd:YAG laser, yielding 403 nm radiation, which was subsequently mixed with the 312.85 nm laser. Finally, 11.9 eV photons were produced by either tripling the output of the 312.85 nm laser in a collinear geometry, or by mixing the 312.85 nm laser with the doubled output (~312 nm) of the second DCM dye laser in a noncollinear geometry.

III. Results/Discussion

A. Phase matching conditions

In most previous studies employing Hg as the nonlinear medium,[9,10] tight-focusing conditions were employed. The dimensionless phase matching factor, $F'(b\Delta k)$, for tight-focused fundamental beams in heated cells has been discussed in detail.[9,10,40] Briefly, phase matching in a tightly-focused configuration where $b << L$ (the confocal parameter is shorter than the length of the nonlinear mixing medium, as in the case of our heated Hg cell), is described by

$$F'(b\Delta k) = \begin{cases} (\pi b\Delta k)^2 e^{b\Delta k}, & \Delta k < 0 \\ 0, & \Delta k \geq 0 \end{cases} \qquad (1)$$

where b is the confocal parameter and Δk is the phase mismatch between the fundamental and generated radiation, defined as

$$\Delta k = 2\pi[2(n_4 - n_1)\lambda_1^{-1} + (n_4 - n_3)\lambda_3^{-1}] \qquad (2)$$

with n_i being the refractive indices of the respective wavelengths, λ_i.

The situation using a laser vaporization cell for producing the nonlinear medium is similar to the phase matching condition found in pulsed jet mixing experiments, where the condition $b << L$ is not necessarily true, i.e. the confocal parameter of the focused laser beam is *not* much shorter than the length of the mixing medium. Rettner *et al.*[22] suggest that in the case of focusing near a pulsed jet, the phase matching conditions are close to those in plane-wave mixing. In such a case, $F'(b\,\Delta k)$ would take the form

$$F'(b\Delta k) = [(2L/b)\frac{\sin(\Delta kL/2)}{(\Delta kL/2)}]^2 \qquad (3)$$

As a result, optimal phase matching is not limited to regions of negative dispersion, making the addition of negatively dispersive gases for phase matching purposes unnecessary.[22,24] For VUV generation in Hg, it is well-know that VUV can be generated on the high energy side of the atomic resonance, in addition to the low energy side.[9,10]

Phase matching conditions for noncollinear alignment of the fundamental beams at a small angle, θ, has been discussed previously.[26,27,41] The effect of noncollinear alignment of the fundamental beams is evident in the phase mismatch (Δk) term of the phase matching factor, $F'(b\Delta k)$. In the case of $\lambda_1 = \lambda_2 = 312.85$ nm, an additional term is needed for Δk

$$\Delta k_{cross} = \frac{k_1 k_3}{2k_1 + k_3}\theta^2 \qquad (4)$$

Thus, introducing noncollinearity will change the optimal range and peak wavelength for sum-frequency mixing, as has been demonstrated both theoretically and experimentally.[26,41]

B. Ablation Laser Conditions and Timing

The VUV intensities are strongly dependent on the timing of the ablation laser relative to the lasers. For 9.9 eV generation (mixing 312.85 nm and 625 nm), the maximum VUV intensities were observed for ablation laser pulse energies of 9 mJ triggered 18 μs before the dye lasers. However, for decreasing ablation laser pulse energies, the optimal delay between the ablation laser trigger and the dye lasers trigger decreased. For example, the optimum time from the ablation trigger to the dye laser trigger was only 4 μs using ablation pulse energies of ~2 mJ. In general, for less efficient schemes producing lower VUV pulse intensities, the maximum VUV intensities were observed with shorter delays between the ablation laser trigger and dye lasers trigger. For example, the optimum delay was ~7 μs for 121 nm and 112 nm generation. For tripling 312.85 nm to make 104.3 nm, optimal delay was ~5 μs. For a given VUV wavelength, the optimal ablation laser timing was found to be the same for both collinear and noncollinear geometries. The mercury vapor density in the plume was not measured directly, but is assumed to be similar to the density of $5x10^{16}$ atoms/cm^3 estimated by Chénais *et al.* in their experiment.[33] Atomic densities in heated cells are also typically 10^{16}-10^{17} atoms/cm^3.

C. Schemes employing the 7 $^1S_0$ two-photon resonance

1. 9.9 eV (125 nm)

When λ_3 is tuned to 623.6 nm, the 9 $^1P_1$ resonance (79,963.85 cm^{-1})[42] is accessible for resonance enhancement. The efficiency for VUV generation near 125 nm using the ablation cell is compared to that for the heated cell in Fig. 2.4. The usable VUV intensity employing the ablation cell is about 80% of that using the heated cell. However, the tuning

curves near the 9 $^1P_1$ resonance differ considerably. For the heated cell, the shape of the tuning curve is in good agreement with previously observed tuning curves.[9,10] The resonance enhancement near the 9 $^1P_1$ resonance using ablation is much broader than using the heated cell. Also, when using the ablation cell, the VUV intensity does not decrease as sharply with increasing crossing angle as in the heated cell. The use of a window in the heated cell reduces photon flux by about 20% at 125 nm. Thus the ablation cell produces about 65% as many VUV photons as the heated cell at 125 nm. However, the number of usable photons produced is the quantity of practical interest. Consequently, VUV intensities are described in terms of "usable photons" rather than the absolute number of photons produced per pulse in the case of the heated cell. In the ablation cell, since no window is required, "usable photons" and "absolute photons" are the same. Using the two-plate detector we calculate $5x10^{12}$ photons/pulse near 125 nm under optimal collinear conditions with the ablation cell. This is about an order of magnitude smaller than we produce using collimated lasers in a 1 m long Hg cell.[11]

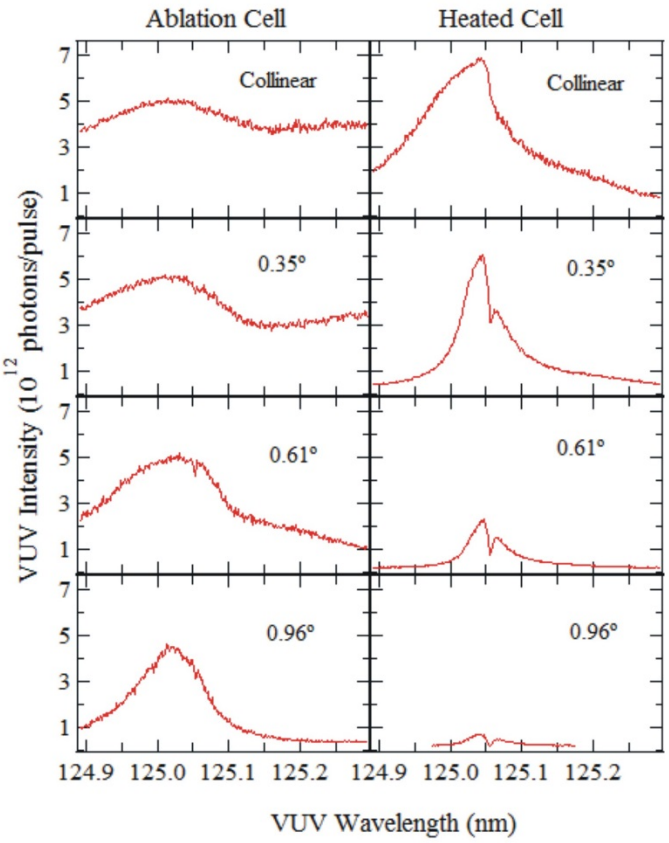

Figure 2.4: Tuning curves around the 9 $^1P_1$ resonance (5.5 mJ/pulse @ 312.85 nm, 5 mJ/pulse @ 625 nm, 7.5 mJ/pulse @ 532 nm).

Chénais *et al.* reported the dependence of the "enhancement ratio", defined as the ratio of the VUV intensity with the vaporization laser on relative to that with the vaporization laser off, as a function of UV, visible, and ablation laser beam pulse energies.[33] We have carried out similar experiments, but instead report the relative intensity of the VUV generated as functions of the three input laser pulse energies, shown in Fig. 2.5. Figure 2.5a shows a linear dependence on 312.85 nm pulse energy up to ~4.5 mJ/pulse, after which the VUV intensity begins to plateau. Figure 2.5b shows that the VUV intensity begins to level off at even lower 623.6 nm pulse energies. For the ablation laser there is a low energy threshold, below which little or no VUV is generated as seen in Fig. 2.5c.

Above this VUV intensity increases with input pulse energies up to ~9 mJ/pulse. The VUV intensity does not increase significantly with further increases in ablation laser pulse energy. Chénais *et al.* attribute this effect to laser energy being shielded by the generated plasma, termed "plasma shielding".[33,43]

At high ablation pulse energies (>10 mJ/pulse), we observed buildup of liquid Hg on entrance windows to the cell. However, at ablation laser pulse energies of 7 mJ/pulse or less, no Hg buildup was observed even after >100 hours of operation. As shown in Fig. 2.5, the VUV pulse intensities plateau at lower pulse energies than in the standard heatpipe configuration in either a focused or unfocused geometry.[9,11,13] To date we have not studied the effect of using achromatic focusing lenses with different focal lengths. Since VUV conversion efficiencies can be high even using unfocused lasers (2 mm dia. beam), it is likely that higher VUV intensities using an ablation source could be produced using higher input pulse energies and a larger beam waist produced by a longer (e.g., 50-60 cm) focal length lens.

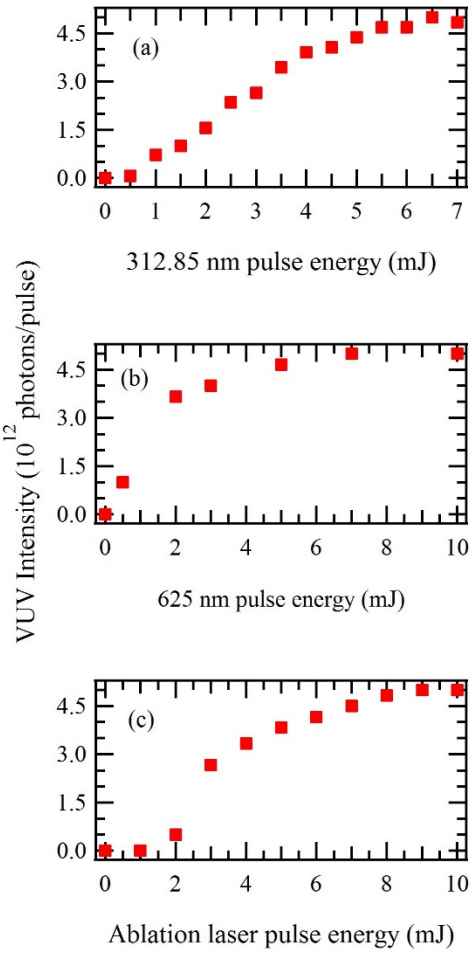

Figure 2.5: VUV intensity vs. (a) 312.85 nm pulse energy (5 mJ/pulse @ 625 nm, 7.5 mJ/pulse @ 532 nm), (b) 625 nm pulse energy (5.5 mJ/pulse @ 312.85 nm, 7.5 mJ/pulse @ 532 nm), (c) ablation laser pulse energy (5.5 mJ/pulse @ 312.85 nm, 5 mJ/pulse @ 625 nm). The ablation laser was triggered 12 μs before the UV and visible lasers.

2. 10.2 eV (121.3 nm)

Tuning λ_3 near λ = 539.5 nm accesses the 12 $^1P_1$ state at 82,463.9 cm^{-1} (121.3 nm).[42] We measured $2x10^{11}$ photons/pulse at this VUV wavelength. The decrease in efficiency upon tuning to higher energy resonances has been reported previously by Hilbig *et al.* and Mahon *et al.*[9,10] Tuning curves around the 12 $^1P_1$ resonance are shown in Fig. 2.6. The curves on the left side employed collinear input beams; the tuning curves on the right side were recorded using a crossing angle of 0.59˚. The shapes of the tuning curves were

affected by the delay between Hg vaporization and VUV pump beams and by the crossing angle of the two incident laser beams. For longer delays between the ablation and VUV lasers, the tuning curve peaks more sharply near the 12 $^1P_1$ resonance. Also, as seen in the case of the 9 $^1P_1$ resonance, the conversion efficiency decreases and the resonance enhancement becomes more sharply peaked for noncollinear geometries.

The constant contribution from the signals resulting from frequency tripling of the 312.85 nm beam (producing 104.3 nm light, as discussed below) has been subtracted from the data shown in Fig. 2.6. This background was most prevalent using collinear beams and short delays between ablation laser and dye laser triggers. At short ablation laser delay times and collinear alignment, the propene photoionization signal from 104.3 nm light was ~35% of the signal produced using two input beams (121.3 nm). For longer delays between ablation laser and dye laser triggers and employing a noncollinear geometry, the 104.3 nm background contribution was typically ~3%.

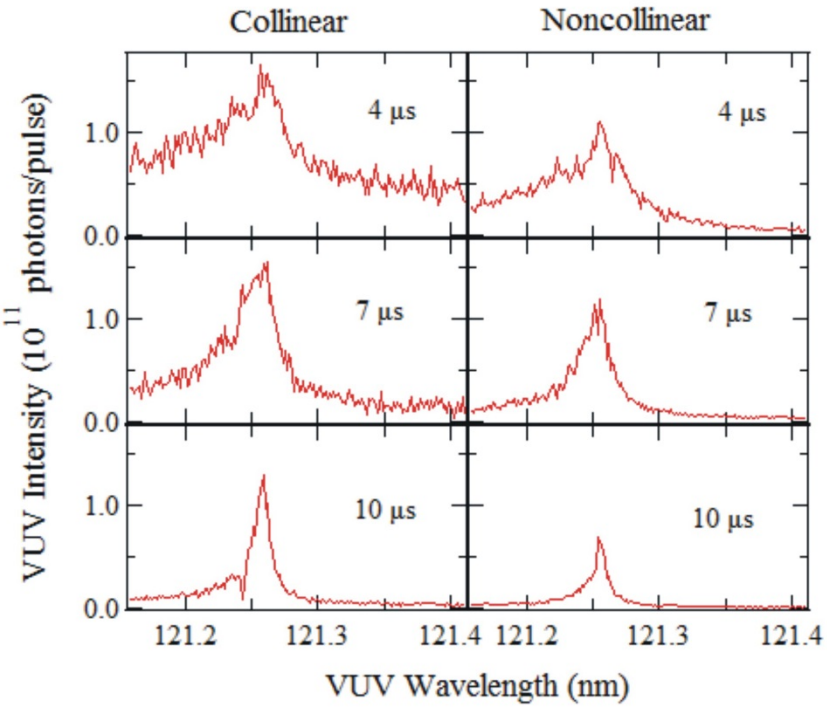

Figure 2.6: Left: collinear scans, ablation laser triggered 4, 7, and 10 µs before the UV and visible lasers (top to bottom). Right: 0.59˚ crossing angle with same ablation laser timing. Laser pulse energies: 2.0 mJ @ 312.85 nm, 2.0 mJ @ 540 nm, and 7 mJ of 532 nm ablation.

Figure 2.7 illustrates how intensities at 121.3 nm varied with input laser pulse energies, with the ablation laser triggered 7 µs before the input laser beams. As the 312.85 nm laser pulse energy was increased, the VUV intensity began to plateau above 1.0 mJ/pulse. On the other hand, a linear dependence was observed for the 540 nm laser up to 4.0 mJ/pulse. As was seen for the generation of VUV at 125 nm, the plot of VUV intensity vs. ablation laser pulse energy shows a threshold below which very little VUV was generated. Over the interval ranging from 3 - 6 mJ/pulse, a relatively linear dependence was observed, reaching a plateau near 8 mJ/pulse.

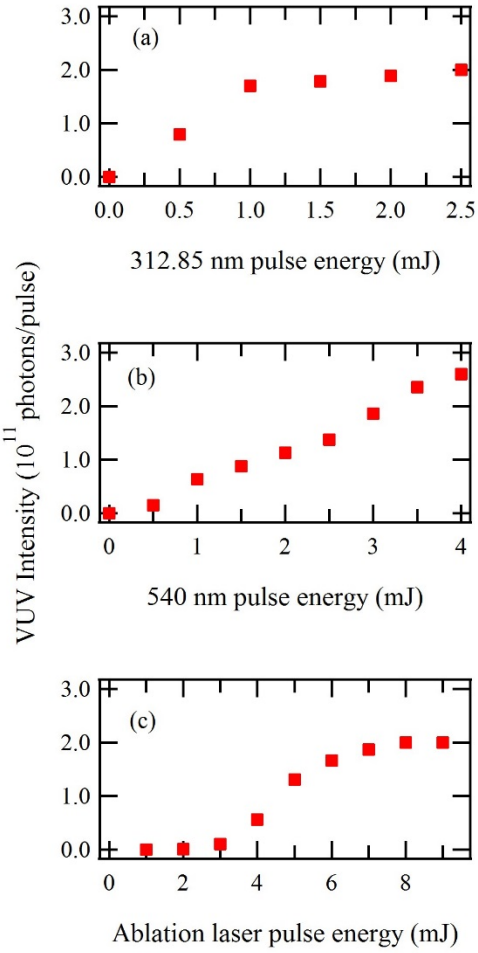

Figure 2.7: VUV intensity vs. (a) 312.85 pulse energy (2.5 mJ/pulse @ 540 nm, 6.5 mJ/pulse @ 532 nm), (b) 540 pulse energy (2.5 mJ/pulse @ 312.85 nm, 6.5 mJ/pulse @ 532 nm), (c) ablation laser pulse energy (2.5 mJ/pulse @ 312.85 nm, 2.5 mJ/pulse @ 540 nm). The ablation laser was triggered 7 μs before the UV and visible lasers.

Pulsed radiation at the Hydrogen Lyman-α (121.6 nm) transition is close in energy to the VUV generated by this scheme, and has been the focus of many previous studies.[1,3,6,7] Nonlinear mixing mediums *other than mercury* (most notably Kr with Ar for phase matching) have been used to generate up to 4.3×10^{12} photons/pulse.[7,44] Even when accounting for losses due to optical elements, schemes employing rare gases provide higher

intensity at Lyman-α than our ablated Hg source.[7] Hg has previously been used as a nonlinear mixing medium for generating *continuous* VUV at 121.6 nm, yielding $3x10^8$ photons/second.[8] Eikema *et. al.* used 257 nm and 399 nm lasers to reach the 7 $^1S_0$ resonance in Hg, similar to the method we describe below, and then 545 nm to produce 121.6 nm radiation (Lyman- α). They also produced 121.6 nm using two photons at 280 nm to reach the 6 ^{1,3}D resonances and a third photon at 915 nm utilizing the 12 $^1P_1$ resonances in Hg.

3. 11.0 eV (112 nm)

Using the 7 $^1S_0$ two-photon resonance, $\lambda_3 \sim 403$ nm produces VUV wavelengths near 112 nm (~88,700 cm^{-1}). According to the NIST atomic database, the $5d^96s^2(^2D_{3/2})6p$ $^2[1/2]_1$ state lies at 88,759.6 cm^{-1}.[42] Since this lies above the Hg ionization limit, no sharp peak is present, although some enhancement is observed in the vicinity of the resonance. With the available laser pulse energies (3 mJ/pulse at 312.85 nm, 5 mJ/pulse at 403 nm), $2x10^{11}$ photons/pulse was measured at 112 nm. Higher input pulse energies would likely increase the VUV intensities in this energy range. Figure 2.8 shows the dependence of the VUV intensity on input pulse energies. The dependence on the 403 nm laser pulse energy is linear, suggesting that a higher pulse energies would lead to increased VUV intensities. As before, a lower limit is seen for the ablation laser pulse energy, as well as a plateau above 6 mJ/pulse.

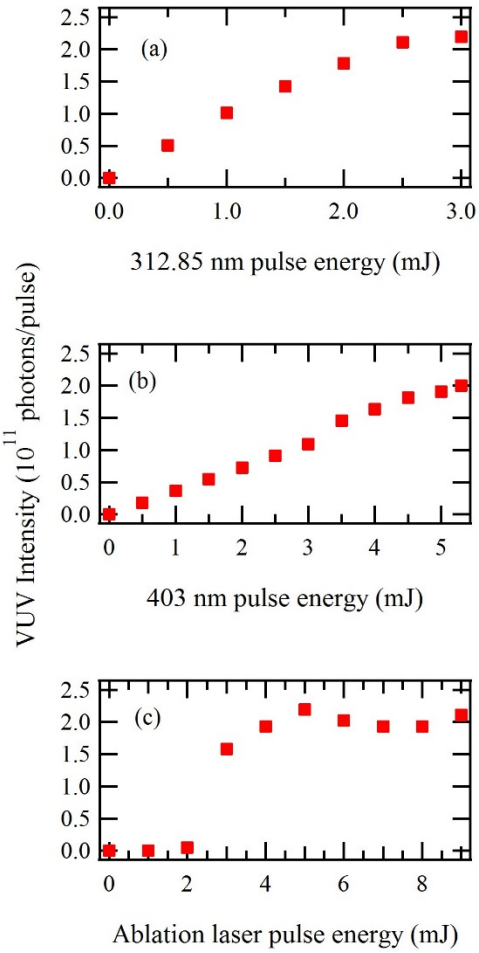

Figure 2.8: VUV intensity vs. (a) 312.85 nm pulse energy (5.5 mJ/pulse @ 403 nm, 6.5 mJ/pulse @ 532 nm), (b) 403 nm laser (3.0 mJ/pulse @ 312.85 nm, 6.5 mJ/pulse @ 532 nm), and (c) ablation laser pulse energy (3.0 mJ/pulse @ 312.85 nm, 5.5 mJ/pulse @ 403 nm). The ablation laser was triggered from 5-9 μs before the UV and visible lasers.

An alternative method for reaching energies near 88,700cm^{-1} utilizes the single photon resonance enhancement afforded by the 6 $^3P_1$ state at 253.7 nm. In this case, a photon near 408 nm reaches the same 7 $^1S_0$ two-photon resonance as two photons at 312.85 nm. The third photon for four-wave mixing can be either a second 253.7 nm or 408 nm photon to give 12.8 eV or 11 eV VUV, respectively. Tuning very close to the 253.7 nm resonance results in strong absorption by Hg, leading to decreased VUV generation. However, tuning to either side of the 253.7 nm resonance results in increased VUV

intensities, with the maximum VUV observed 30 cm^{-1} to 200 cm^{-1} below the 6 $^3P_1$ state, corresponding to $\lambda_1 \sim 254$ nm. Using 0.8 mJ/pulse at 254 nm and 4.5 mJ/pulse at 408 nm, two different wavelengths were produced, 96.9 and 113 nm, corresponding to photon energies of 12.8 and 11 eV. By photoionizing a molecular beam of acetylene (ionization energy of 11.4 eV), we measured the intensity of the 96.9 nm VUV to be $2x10^8$ photons/pulse. When observing a molecular beam of 1-butene, we measured the total VUV intensity to be $5x10^{11}$ photons/pulse, leading to the conclusion that generation of 113 nm photons is more than three orders of magnitude more efficient than generation of 96.9 nm photons. Figure 2.9 shows VUV intensity vs. 254 nm, 408 nm, and 532 nm pulse energies.

Hilbig and Wallenstein have previously demonstrated VUV generation in this wavelength range, both by nonresonant sum-frequency mixing in krypton leading to 114 nm VUV, and by using the 6 $^1S_0$ – 6 $^1D_2$ two-photon resonance in mercury to generate 112 nm VUV. The VUV intensities produced were $1x10^{10}$ and $5x10^{11}$ photons/pulse, respectively.[2,9] Accounting for the transmission of one LiF optic in this wavelength range (<50%), their maximum usable VUV intensities were $5x10^9$ and $2.5x10^{11}$ photons/pulse.

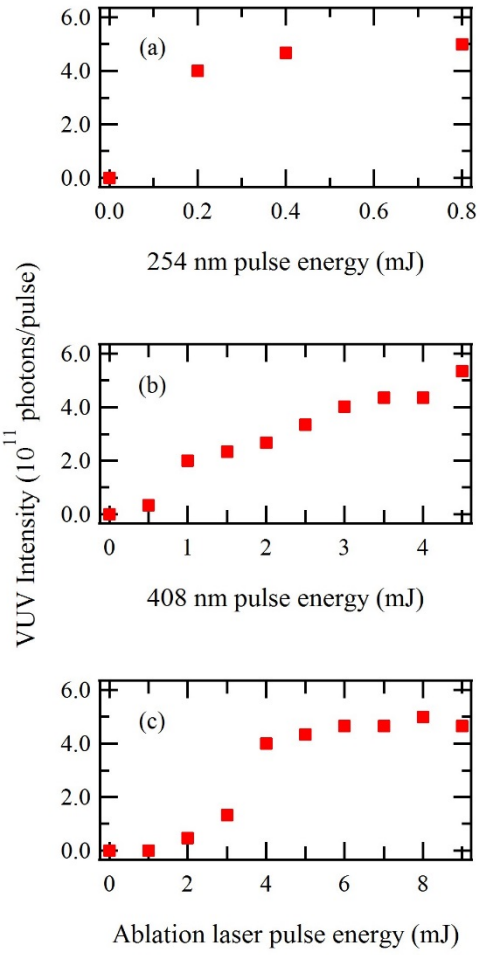

Figure 2.9: VUV intensity vs. (a) 254 nm laser pulse energy (4.5 mJ/pulse @ 408 nm, 6.5 mJ/pulse @ 532 nm), (b) 408 laser pulse energy (0.8 mJ/pulse @ 254 nm, 6.5 mJ/pulse @ 532 nm), and (c) ablation laser pulse energy (0.8 mJ/pulse @ 254 nm, 4.5 mJ/pulse @ 408 nm). The ablation laser was triggered 14 μs before the UV and visible lasers.

4. 11.9 eV (104 nm)

By tripling the 312.85 nm radiation, 11.9 eV photons (104.3 nm, 95,892 cm^{-1}) were produced with quite high efficiencies even though the nearest known resonance ($5d^{10}6p^2$ $^3P_2$) lies at 96,190 cm^{-1}, i.e., 300 cm^{-1} away.[42] Alignment of two 312.85 nm beams with a crossing angle of .67° resulted in intensities approximately half that using the collinear

geometry. By generating the second 312 nm beam with a second dye laser, we scanned λ_3 and looked for resonance enhancements, but none were observed. The maximum absolute intensity of this scheme under collinear conditions was $4x10^{10}$ photons/pulse. Production of VUV at 104.3 nm has been observed previously, but intensity measurements were either not reported,[10,19] or VUV was generated in a heated cell with no window connected directly to a detector under a few torr of He,[10] in which case Mahon and Tomkins measured $4x10^{10}$ photons/pulse under tight focusing conditions. Kwon *et al.* measured the VUV intensity for mixing two photons at 312.85 nm and a third photon ranging from 320-355 nm and reported a usable photon intensity of $4x10^9$ photons/pulse.[19] Marinero *et al.* report $7x10^9$ photons/pulse from 100 to 102.3 nm by frequency tripling in a pulsed Ar gas source.[45] Cromwell *et al.* reported XUV peak intensities of $>10^{11}$ around 98 nm when using resonance enhanced mixing of a pulse amplified ring laser in a pulsed beam of Ar.[24] This XUV intensity is similar to the maximum 104 nm intensity we were able to generate using commercial dye lasers when the Hg mixing region volume was increased, as discussed below.

Figure 2.10 shows 104 nm intensities as a function of input laser pulse energies in collinear geometry. Figure 2.10a shows a clear saturation above 2 mJ/pulse for the input 312 nm power, similar to the trends observed in both 125 nm and 121 nm generation. As seen in Fig. 2.10b, for 104 nm production a threshold is observed for the ablation laser pulse energy followed by a liner VUV intensity increase. We observed no plateau in 104 nm intensity for high ablation laser pulse energies.

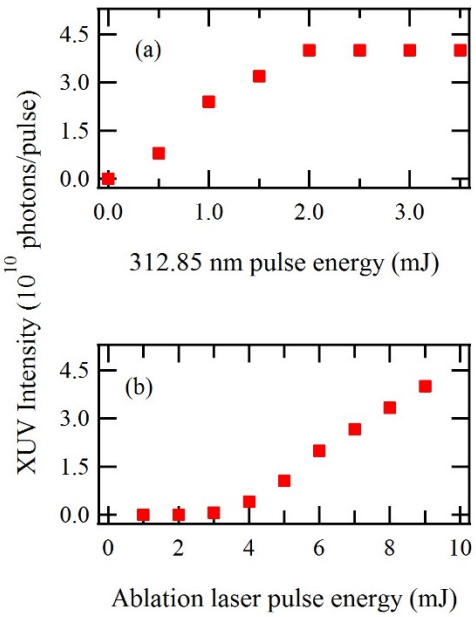

Figure 2.10: VUV intensity vs. (a) 312.85 nm laser pulse energy (6.5 mJ/pulse @ 532 nm), and (b) ablation laser pulse energy (2.5 mJ/pulse @ 312.85 nm). The ablation laser was triggered 5 μs before the 312.85 nm laser.

D. Schemes employing the 8 $^1S_0$ two-photon resonance

1. 13.8 eV (89.6 nm)

The 8^1S_0 resonance in Hg lies at 74,404 cm^{-1}, accessible by two photons at 268.8 nm.[38] There have been a number of previous studies employing this resonance.[18,20,46] Using a collinear geometry, tripling of the 268.8 nm laser was first optimized, producing light at 89.6 nm (13.8 eV). We found that the XUV intensity at this wavelength is about three orders of magnitude weaker than at 104.3 nm (the analogous scheme using 7^1S_0), i.e., we produced $3x10^7$ photons/pulse at 89.6 nm. This is about an order of magnitude greater than that reported by Herman and Stoicheff.[20] Hannemann *et al.* describe generating 91 nm XUV using four-wave mixing in Kr, and while they did not measure the XUV intensity directly, they estimated 10^9 photons/pulse.[27] Koudoumas and Efthimiopoulos estimated

10^8 photons/pulse generated at this wavelength, but transmission from their mixing region to their detection region was ~5%, i.e., their usable VUV intensity was ~$5x10^6$ photons/pulse.

2. 11.0 eV (112 nm)

By employing the 268.8 nm two-photon resonance, and adding λ_3 ~ 620-710 nm, we observed a large enhancement in VUV production (relative to tripling 268.8 nm to produce 89.6 nm radiation), with no strong dependence on the exact wavelength of λ_3. The use of λ_3 ~ 695 nm produces VUV photons near 11 eV, similar to the scheme involving the 7S resonance employing 312.85nm + 403 nm input beams. We found that the VUV intensities near 11 eV using the 8 $^1S_0$ state to be 10^{10} photons/pulse, a factor of 15-20 smaller than generating the same wavelength using the 7 $^1S_0$ two photon resonance.

E. Schemes employing the 9 $^1S_0$ two-photon resonance

1. 14.6 eV (85 nm)

Two photons at 255.1 nm are resonant with the 9 $^1S_0$ state in Hg, which lies at 78,404.24 cm^{-1}.[42] This two-photon resonance represents another potential route to production of XUV photons using λ_3 in the visible and near UV. Using 0.7 mJ/pulse at 255.1 nm, $6x10^6$ photons/pulse were generated by tripling 255.1 nm to give 85 nm (14.8 eV/photon). Our laser system was not optimized for production of light at 255.1 nm. Since much higher input pulse energies near 255.1 nm could be produced (> 3 mJ), at least an order of magnitude greater XUV intensities in the 14.6 eV range should be easily achievable.

F. Refocusing Using Concave Silicon Mirror

The use of focused input lasers produces divergent VUV and XUV output beams. However, some applications require that the VUV or XUV beam be refocused, requiring the use of reflective optics at wavelengths shorter than 104 nm. According to calculations by Hunter,[47] the reflectivity of silicon at normal (90^o) incidence exceeds 60% in the VUV and XUV region. We have carried out experiments using a 1" diameter Si infrared lens (1 m radius of curvature) as a mirror at near normal incidence in order to recollimate 112 nm light produced by noncollinear mixing of 312.85 nm and 404 nm input beams. Consistent with the calculations, the near-normal reflectance was about 60% at 112 nm. Since highly polished Si lenses and mirrors can be obtained at relatively low cost (e.g., ISP Optics) their use provides a very simple and cost-effective approach for refocusing or recollimating VUV and XUV laser beams.

G. The effect of Increased beam diameter

By using a longer focal length lens for focusing the input beams, the radius of the beam waist, ω_0, is increased according to the relationship $\omega_0 = \left(\frac{4\lambda}{\pi}\right)\left(\frac{f}{d}\right)$, where f is the focal length, d is the laser beam diameter before the lens, and λ is the wavelength. This consequently increases the mixing volume. Using input pulse energies of 7 mJ at 312.85 nm, by replacing the 34 cm focal length achromatic lens with a 53 cm focal length lens, the λ=104 nm XUV intensity doubled to 7×10^{10} photons/pulse. However, after making the same change for production of light at λ=125 nm (using 7 mJ at 312.85 nm + 11 mJ at 623.6 nm), the output pulse energy decreased, most likely due to the poorer spatial overlap resulting from the use of a nonachromatic lens.

H. Ablation of a Line

In an effort to increase the length of the mixing region, we replaced the spherical lens focusing the ablation laser with a 25 cm focal length cylindrical lens. This allowed ablation of a 1 mm x 10 mm line of mercury rather than a 2 mm dia. spot. Using this configuration, we tested both 104 nm and 125 nm generation. Intensity at 104 nm was about 20% greater ($9x10^{10}$ photons/pulse) using the cylindrical lens compared to that using the 40 cm FL spherical lens. At 125 nm, the VUV intensity decreased by a factor of two, likely because the 53 cm lens was not achromatic. However, the power dependences of both the 312.85 nm and 623.6 nm radiation were linear at pulse energies up to 7 mJ/pulse at 312.85 nm and 11 mJ/pulse at 623.6 nm. These results suggest that higher pulse energies, a cylindrical lens for ablation, and an achromatic lens for the input beams could lead to increased VUV intensities.

I. Photoionization threshold of CH_3Br

We have tuned the VUV source to the photoionization threshold of methyl bromide, CH_3Br, which has a well established ionization energy of 10.541 ±.003 eV.[48] Using noncollinear mixing of 312.85 nm photons with 474.7 nm photons, the observed appearance energy of CH_3Br^+ observed by photoionization of a molecular beam containing .5% CH_3Br in He was within the currently accepted range. (Fig. 2.11)

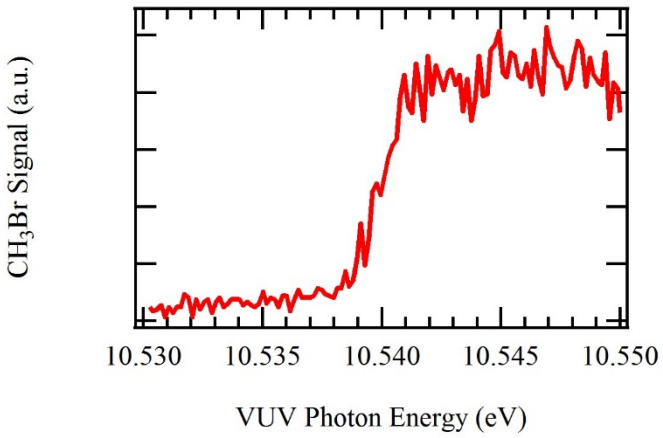

Figure 2.11: Photoionization threshold of CH_3Br, where λ_3 is scanned from 472.7 – 476.7 nm. The observed ionization threshold of 10.539 eV is within the uncertainty of the accepted value of 10.541 ± .003 eV.

IV. Conclusions

We have developed and characterized an approach for generating VUV and XUV radiation by resonance enhanced four-wave sum-frequency laser mixing in laser vaporized Hg. Noncollinear mixing makes it possible to eliminate all optical elements following VUV or XUV generation, facilitating windowless operation with spatial separation of the beams. Compared to the use of heated Hg cells, the use of laser vaporization also leads to broader tuning curves due to less restrictive phase matching conditions near Hg atomic resonances. We have produced radiation in the 9.9 eV – 14.6 eV range, and highlight a convenient approach allowing rapid access to three different wavelengths corresponding to photon energies of 10, 11, and 12 eV.

The usable VUV intensities we have generated at various wavelengths, particularly for photon energies > 11 eV, are in most cases greater than the usable photon intensities demonstrated previously. Near 11 eV, we measured a factor of two greater usable photon intensity ($5x10^{11}$ photons/pulse).[9] At 104 nm (12 eV), our usable VUV intensity of $9x10^{10}$

photons/pulse, is similar to a previous estimate of ~10^{11} photons/pulse using a much more complex laser system.[24] At 89.6 nm (13.8 eV), we generated an order of magnitude more VUV than previously measured using Hg as a nonlinear mixing medium at that wavelength.[20]

The Nd:YAG pumped dye laser system employed in this work is very modest by present-day standards. Using more modern commercially-available pulsed lasers, input pulse energies 10 times higher than those used here are readily achievable. Therefore, with some effort, much higher pulse energies in the VUV and XUV are readily achievable using the methods described here.

V. References

1. J. W. Hepburn, "Applications of Coherent Vacuum Ultraviolet to Photofragment and Photoionization Spectroscopy," in *Vacuum Ultraviolet Photoionization and Photodissociation of Molecules and Clusters*, C.Y. Ng, ed. (World Scientific, Singapore, 1991) pp. 435-485.
2. R. Hilbig and R. Wallenstein, *Appl. Opt.* **21**, 913 (1982).
3. R. Mahon, T. J. McIlrath, V. P. Myerscough, and D. W. Koopman, *IEEE J. Quantum Electron.* **15**, 444 (1979).
4. K. S. E. Eikema and W. Ubachs in *Handbook of High Resolution Spectroscopy*, edited by M. Quack and F. Merkt (John Wiley & Sons, 2010) pp. 1374-1413.
5. R. Hilbig and R. Wallenstein, *IEEE J. of Quantum Electron.* **19**, 194 (1983).
6. H. Langer, H. Puell, and H. Roehr, *Opt. Commun.* **34**, 137 (1980).
7. J. P. Marangos, N. Shen, H. Ma, M. H. R. Hutchinson, and J. P. Connerade, *J. Opt. Soc. Am.*, **7**, 1254 (1990).
8. K. S. E. Eikema, J. Walz, and T. W. Hänsch, *Phys. Rev. Lett.* **83**, 3828 (1999).
9. R. Hilbig and R. Wallenstein, *IEEE J. Quantum Electron.* **19**, 1759 (1983).
10. R. Mahon and F. S. Tomkins, *IEEE J. Quantum Electron.* **18**, 913 (1982).
11. D. R. Albert, D. L. Proctor, and H. F. Davis, *Rev. Sci. Instrum.* **84**, 063104 (2013).
12. A. V. Smith and W.J. Alford, *J. Opt. Soc. Am. B* **4**, 1765 (1987).
13. C. H. Muller III, D. D. Lowenthal, M. A. DeFaccio, and A.V. Smith, *Opt. Lett.* **13**, 651 (1988).
14. W. A. VonDrasek, S. Okajima, and J. P. Hessler, *Appl. Opt.* **27**, 4057 (1988).
15. R. R. Smardzewski, *Appl. Spectrosc.* **31**, 332 (1977).

16. T. B. Lucatorto, T. J. McIlrath, and J. R. Roberts, *Appl. Opt.* **18**, 2505 (1979).

17. L. Hellner and J. Lukasik, *Opt. Commun.* **51**, 347 (1984).

18. E. Koudoumas and T. Efthimiopoulos, *Laser Chem.* **13**, 129 (1993).

19. C. H. Kwon, H. L. Kim, and M. S. Kim, *Rev. Sci. Instrum.* **74**, 2939 (2003).

20. P. R. Herman and B. P. Stoicheff, *Opt. Lett.* **10**, 502 (1985).

21. A. H. Kung, *Opt. Lett.* **8**, 24 (1983).

22. C. T. Rettner, E. E. Marinero, R. N. Zare, and A. H. Kung, *J. Phys. Chem.* **88**, 4459 (1984).

23. R. H. Page, R. J. Larkin, A. H. Kung, Y. R. Shen, and Y. T. Lee, *Rev. Sci. Instrum.* **58**, 1616 (1987).

24. E. Cromwell, T. Trickl, Y. T. Lee, and A. H. Kung, *Rev. Sci. Instrum.* **60**, 2888 (1989).

25. U. Hollenstein, H. Palm, and F. Merkt, *Rev. Sci. Instrum.* **71**, 4023 (2000).

26. V. E. Peet and R.V. Tsubin, *Opt. Commun.* **214**, 381 (2002).

27. S. Hannemann, U. Hollenstein, E.-J. van Duijn, and W. Ubachs, *Opt. Lett.* **30**, 1494 (2005).

28. J. Darginavičius, G. Tamošauskas, G. Valiulis, A. Dubietis, *Opt. Comm.* **282(4)**, 2995 (2009).

29. J. Darginavičius, G. Tamosauskas, A. Piskarkas, A. Dubietis, *Opt. Express* **18**, 16096 (2010).

30. J. L. Silva, H. Crespo, and R. Weigand, *Appl. Opt.* **50**, 1968 (2011).

31. Rosa Weigand and Helder M. Crespo, *Applied Physics B* **111**, 559 (2013).

32. R. Hector and K. H. Meiwes-Broer, *Opt. Commun.* **123**, 155 (1996).

33. S. Chénais, S. Forget, L. Philippet, and M.-C. Castex, *Appl. Phys. B* **89**, 223 (2007).

34. M. L. Huber, A. Laesecke, and D. G. Friend, NISTIT 6643, Boulder, CO, (2006).

35. L. Museur, W. Q. Zheng, A.V. Kanaev, and M. C. Castex, *IEEE J. Sel. Top. Quant. Elect.*, **1**, 900 (1995).

36. L. Museur, C. Olivero, D. Riedel, and M. C. Castex, *Appl. Phys. B.* **70**, 499 (2000).

37. J. Wang, B. Yang, T. A. Cool, N. Hansen, and T. Kasper, *Int. J. Mass Spectrom.* **269,** 210 (2008).

38. J. C. Person and P. P. Nicole, *J. Chem. Phys.* **53**, 1767 (1970).

39. N. Bras, J.C. Jeannet, and D. Perrin, *J. Phys. B* **26**, 2289 (1993).

40. G. C. Bjorklund, *IEEE J. Quantum Electron.* **11**, 287 (1975).

41. A. V. Smith and W. J. Alford, *Phys. Rev. A* **33**, 3172 (1986).

42. A. Kramida, Y. Ralchenko, J. Reader, and NIST ASD Team (2012). *NIST Atomic Spectra Database* (ver 5.0), [Online]. Available: http://physics.nist.gov/asd [2013, July 5]. National Institute of Standards and Technology, Gaithersburg, MD.

43. A. Bogaerts, Z. Y. Chen, R. Gijbels, and A. Vertes, *Spectrochimica Acta Part B.***58**, 1867 (2003).

44. S. A. Meyer and G. W. Faris, *Opt. Lett.* **23**, 204 (1998).

45. E. E. Marinero, C. T. Rettner, R. N. Zare, and A. H. Kung, *Chem Phys. Lett.* **95**, 486 (1983).

46. V. V. Slabko, A. K Popov, and V. F. Lukinykh, *Appl. Phys.* **15**, 239 (1977).

47. W. R. Hunter, "Reflectance Spectra of Single Materials," in *Vacuum Ultraviolet Spectroscopy*, J. A. Samson and D. L. Ederer (Academic Press, San Diego, 2000) pp. 205-225.

48. S. G. Lias, “Ionization Energy Evaluation” in **NIST Chemistry WebBook, NIST Standard Reference Database Number 69**, Eds. P. J. Linstom and W. G. Mallard, Nation Institute of Standards and Technology, Gaithersburg MD, 20899, http://webbook.nist.gov, (retrieved September 30, 2015).

CHAPTER 3

I + O_2 PRODUCTION FROM THE PHOTODISSOCIATION OF OIO

I. Introduction

The halogen oxide diatomic radicals IO, BrO, and ClO play key roles in atmospheric chemistry, most notably in polar ozone depletion.[1,2,3,4,5,6,7] The IR and UV spectroscopies of these molecules have been studied extensively over many decades.[2,8] Whereas ClO photodissociation has been studied for more than 15 years, [9,10,11] analogous studies on BrO[12] and IO[13] have only appeared recently.

The diatomic IO molecule, produced by oxidation of naturally-occurring iodine compounds in the atmosphere, has been observed in the marine boundary layer. Iodine can participate in catalytic cycles similar to that for Cl and Br.[14] It is believed that reactions involving IO with itself,[15] BrO[16], and ClO[17,18] all produce OIO, but the branching ratios are subject to uncertainty.

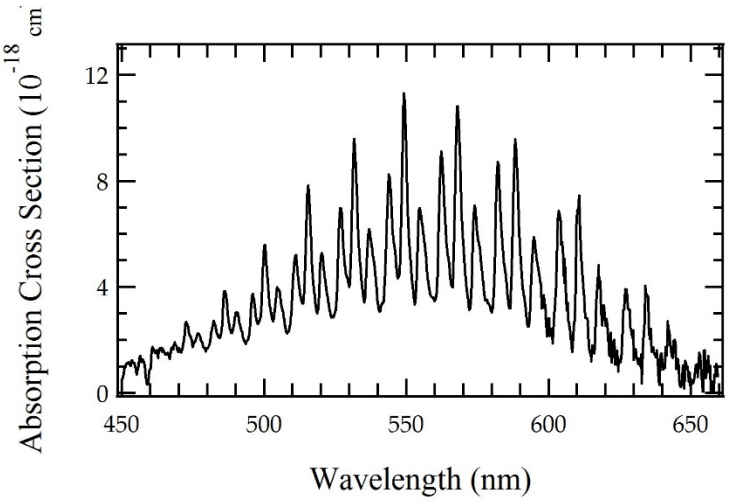

Figure 3.1: OIO electronic absorption spectrum from 450-660 nm, reproduced using data from Ref. 20.

Himmelman *et al.*[19] were the first to study the electronic absorption spectroscopy of OIO.[20,21,22,23] The absorption spectrum shown in Figure 3.1 is reproduced using data from Spietz *et al.*[20] Like OClO and OBrO, OIO has a very strong structured absorption spectrum throughout the visible region with its band origin near 687 nm. Since fluorescence emission has been found to be absent, two different OIO photodissociation pathways could be operative. [20,23,24]

$$OIO + h\nu \rightarrow IO + O \quad (1a)$$

$$\rightarrow I + O_2 \quad (1b)$$

Whereas the IO + O channel leads to production of odd oxygen and a net null cycle in the balance of atmospheric ozone, the $I + O_2$ channel, if important, could represent a pathway for catalytic conversion of O_3 to O_2, decomposing two ozone molecules for every cycle:

$$2(I + O_3 \rightarrow IO + O_2) \quad (2)$$

$$IO + IO \rightarrow OIO + I \quad (3)$$

$$\underline{OIO + h\nu \rightarrow I + O_2} \quad (1b)$$

$$\text{Net: } 2O_3 \rightarrow 3O_2$$

There have been a number of previous experimental studies of OIO photochemistry. Cox *et al.* tried to observe evidence for OIO photodissociation and concluded that OIO was photochemically stable.[25] A short time later, Ingham *et al.* studied photolysis of OIO at 532 nm[23] and observed $I(^2P_J)$, but interpreted it as a two-photon processes and reported a quantum of less than 0.1 for $I + O_2$ production. Ashworth *et al.* observed loss of OIO upon absorption of visible light. Calculations suggested that the likely products were $I + O_2$ as opposed to O + IO.[26] Joseph *et al*. observed μs timescale recovery

of ground state OIO upon absorption in a cavity ring-down experiment, attributed to fast internal conversion to high vibrationally excited levels of the $^2B_1$ ground state.[24] They reported a small quantum yield for I + O_2 production, with an upper limit of 10% OIO dissociation at 562 nm. Experiments by Tucceri *et al.*[22] further supported the photostability of OIO, and an upper limit of 0.24 was derived for the photodissociation quantum yield at 532 nm. In contrast, Gómez Martín *et al.*[20] later observed photodissociation of OIO yielding I + O_2, and reported a quantum yield of 1.07 ± .15 from 513-640 nm. In a separate study, Gómez Martín and Plane determined that the wavelength threshold for O + IO production was 480.8 ±2 nm[27] leading them to conclude that D_0(O-IO) = 248.8 ± 1.0 kJ/mol.

Peterson carried out detailed calculations on the low-lying electronic states of OIO, OIO^-, and IOO.[28] Upon excitation to the C^2A_2 state, OIO is expected to predissociate through the B^2A_1 state. As in the case of OClO, vibronic interactions lead to involvement of the A^2B_2 state in the dissociation dynamics. Dissociation of OIO can produce I ($^2P_{3/2}$) + O_2 with significant populations of both ground state O_2 ($^3\Sigma_g^-$) and excited O_2 ($^1\Delta_g$). According to the calculations, the reaction OIO → I($^2P_{3/2}$) + O_2 involves a large potential and is exoergic by -3.27 kcal/mol. While the possibility for production of electronically excited I($^2P_{1/2}$) was not addressed in the theoretical work, or in previous experiments, it is energetically accessible at all OIO absorption wavelengths if accompanied by formation of ground state O_2 ($^3\Sigma_g^-$). A correlation diagram for low lying electronic states of OIO and various dissociation pathways calculated by Petersen is reproduced in Figure 3.2.[28]

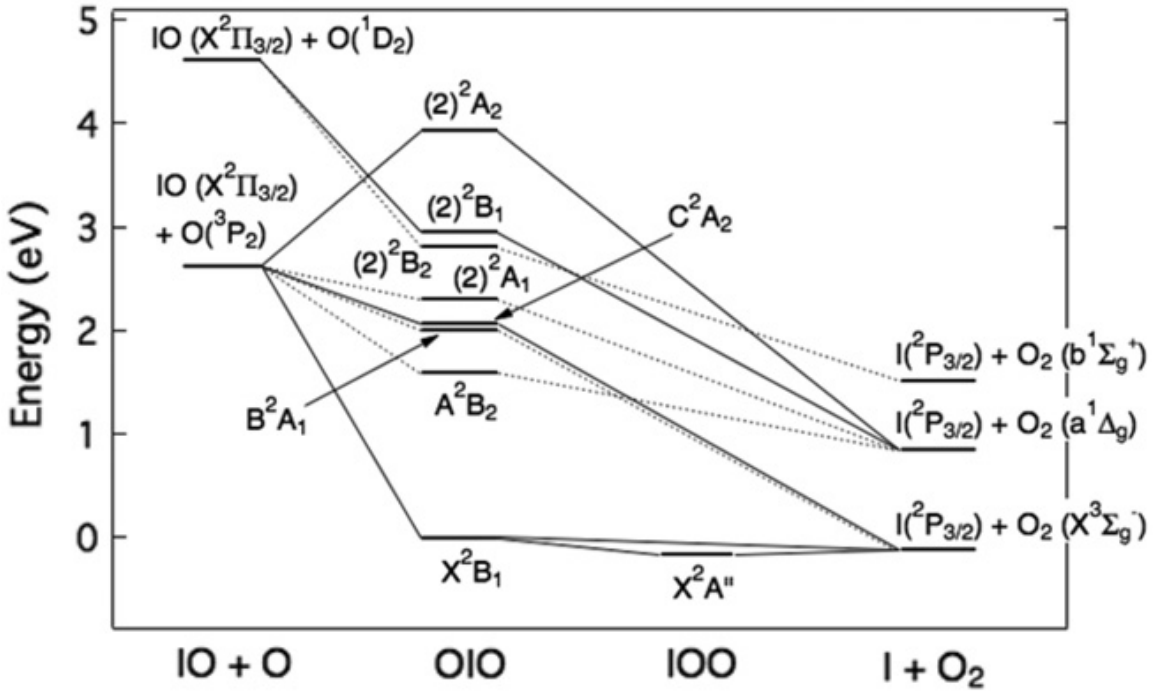

Figure 3.2: OIO correlation diagram showing the energy differences and various dissociation pathways correlated to each excited state, reproduced from Ref. 28.

As discussed in a recent review of gas phase iodine chemistry, further experiments on these and related systems are desirable.[29] We have studied the dynamics of OIO photodissociation producing $I(^2P_{3/2}) + O_2$ at a four wavelengths longer than the reported threshold for O + IO production: 635 nm, 568 nm, 532 nm, and 486 nm. In addition, we have observed $I + O_2$ production at 473 nm, where the O + IO channel is thought to be energetically accessible. By measuring the translational energy distributions of ground state $I(^2P_{3/2})$, the internal energy distribution of the O_2 counterfragments were deduced.

II. Experimental

The experiments were carried out using the Cornell rotatable source crossed molecular beams apparatus, discussed in Chapter 1 and in more detail elsewhere.[30] The OIO molecular beam was produced through the reaction OI + OI → OIO + I in a quartz tube reactor. The OI was produced by photolysis of O_3 mixed with CF_3I at 266 nm using the fourth-harmonic output of a Nd:YAG laser (Continuum 8020). The laser was mounted to and rotated with the source in order to maintain alignment. Ozone was produced by a commercial ozone generator and trapped in a silica gel trap held at -78° C. By passing helium gas through the trap, thermostatically held at -45° C, an ozone concentration of ~1% in He was produced at a total pressure of ~900 Torr. The ozone mixture and CF_3I mixtures (10% in He, ~1000 Torr) were delivered and mixed *in situ* from separate piezoelectrically actuated pulsed valves, as illustrated in Figure 3.3. A quartz reactor tube, 5 cm long, 3 mm O.D. and 2 mm I.D. was attached to the nozzle. The CF_3I/O_3 mixture was photolyzed within the quartz tube approximately 4 cm upstream of its exit. Upon photolysis, O_3 dissociates predominantly to form $O(^1D_2)$, which is subsequently quenched to $O(^3P)$ and reacts with an excess of CF_3I to produce IO. The IO self-reaction occurs as the gas mixture travels through the remainder of the tube, yielding OIO. Following supersonic expansion from the end of the quartz tube, the molecular beam passes through a differentially pumped region and was collimated by two skimmers. The photodissociation laser was either the fundamental output from a Nd:YAG pumped Lambda-Physik Scanmate 2 dye laser (0.1 cm^{-1} bandwidth), or the second harmonic 532.1 nm of a Nd:YAG laser (1 cm^{-1} bandwidth).

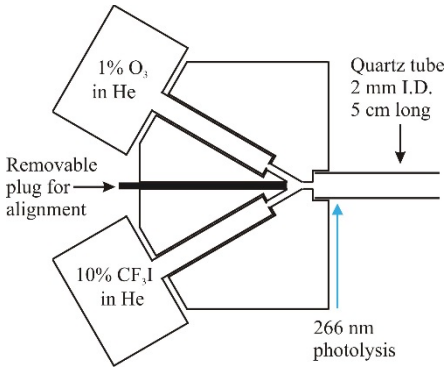

Figure 3.3: Illustration of dual pulsed valve mount for OIO generation.

The I($^2P_{3/2}$) products from OIO photodissociation were ionized by two-color excitation through the $5s^25p^4(^3P_2)6d\ ^2[2]_{5/2}$ state, followed by mass selection by a quadrupole mass filter. Vacuum ultraviolet light at 76,903.27 cm^{-1} was produced via sum-frequency resonance-enhanced four wave mixing of unfocussed dye lasers in a long heated Hg cell.[31] The input laser wavelengths for VUV generation were λ_1 = 255 nm, λ_2 = 404 nm, and λ_3 = 770 nm. These wavelengths were chosen to optimize phase matching, as described elsewhere.[31] The second counterpropagating laser beam at 635 nm was spatially and temporally overlapped with the VUV laser in the photoionization region of the detector.

Owing to side reactions occurring in the molecular beam, at some wavelengths I atoms from photodissociation of I_2 impurity were observed. This was most evident at 532 nm and 486 nm, where I_2 absorption cross sections are relatively large. Signals from I_2 dissociation are accounted for explicitly, as discussed below.

The structured absorption spectrum of OIO in the 475-660 nm range has been attributed to transitions from the ground state X(0, 0, 0) to various vibrational levels (v'_1, v'_2, v'_3) of the C^2A_2 excited electronic state, where v'_1, v'_2, and v'_3 correspond to the symmetric stretch, bend and antisymmetric stretching modes, respectively.[19,20,28] In the

case of OIO, the progression involves pure symmetric stretch (e.g., v'_1,0,0) plus either one (v'_1,1,0) or two (v'_1,2,0) quanta of bending excitation. For detection of I($^2P_{3/2}$), $E_{int\ I}$ is zero. Assuming that absorption at each wavelength originates exclusively from OIO (0,0,0) levels (i.e., assuming no hotband absorption), $E_{int\ OIO} = 0$. The question of whether or not hotband activity is zero will be addressed below.

For experiments at small molecular beam angles (e.g., 10°), some I atom background from the molecular beam can be observed starting at flight times t ~ 180 μs. For these laboratory angles, TOF spectra were also recorded with the photolysis laser blocked, and difference TOF spectra employed in the analysis.

III. Results and Discussion

A. IO photodissociation

Bond dissociation energy values can be determined with high precision using photofragment translational energy spectroscopy, demonstrated here comparing independently determining the IO dissociation energy for comparison to similar experiments by Dooley *et al.*[13] In these experiments, IO was generated by 266 nm photolysis of O_3 and CF_3I, similar to OIO generation described above but in a .5 cm quartz tube rather than 5 cm quartz tube. The photodissociation wavelength was tuned to the (3-0) band at 436 nm, and the O($^3P_2$) product was state specifically detected with two color excitation through the $2s^22p^3(^4S°)3s\ ^3S°_1$ state at 76,794.978 cm^{-1}. The bond dissociation energy of IO was previously been determined to be $54.9^{+.2}_{-.4}$ kcal/mol by Dooley *et al.* through detecting I($^2P_{3/2}$) photofragments from dissociation at 454.9 nm on the (1-0) bandhead.[13] Their spectra were subject to broadening of the I arrival time due to the

presence of three O-atom spin orbit states energetically available, ($^3P_{0,1,2}$). In the present experiments, through state specific detection of O($^3P_2$) the only pathway available is with a counterfragment of I($^2P_{3/2}$).

Time-of-flight spectra for IO photodissociation are shown in Figure 3.4. At lab angles of 10° and 40°, forward convolution fits are shown for three different D_0 values. The best fit is achieved with D_0 = 54.87 kcal/mol, well within the uncertainty of Dooley *et al.*[13] The uncertainty of this measurement is illustrated by the green and blue curves. By changing the value of D_0 by ±0.1 kcal/mol there is a clear shift in predicted arrival time. For detection of I atom in OIO dissociation experiments, the uncertainty in the maximum kinetic energy is larger. A conservative estimate of the uncertainty in the I atom kinetic energy release measurements is ±2 kcal/mol.

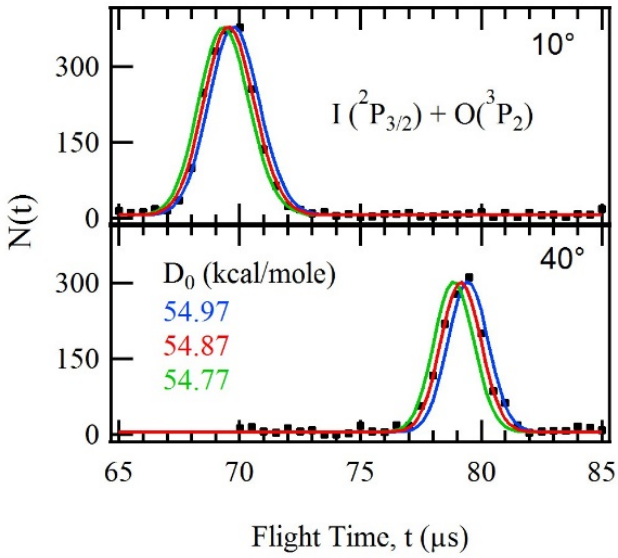

Figure 3.4: TOF spectra for O($^3P_2$) from 436 nm photodissociation of IO at lab angles of 10° and 40°. Black square are experimental data. Red curves show forward convolutions for D_0=54.87 kcal/mol. Green curves are fits using D_0=54.77 kcal/mol, and blue curves are fits using D_0=54.97 kcal/mol.

B. 568 nm

Figure 3.5 shows the TOF spectra of the I($^2P_{3/2}$) product from photodissociation of OIO at 568 nm, the (4,1,0) absorption peak, at the indicated lab angles. The maximum translational energy of the ground state I ($^2P_{3/2}$) products recoiling from ground state O_2 was found to be 55 ± 2 kcal/mol. Assuming $E_{int,\ OIO} = 0$, this corresponds to a reaction exoergicity of -4.7 ± 2 kcal/mol, 1.5 kcal/mole greater than the value of -3.23 kcal/mol calculated by Peterson.[28] Our value also exceeds the exoergicity calculated using the 0 K heat of formation for OIO derived by Gómez Martín and Plane.[27]

The best-fit P(E) shown in Figure 3.6 has a bimodal distribution with the major components separated by ~23 kcal/mol. This behavior is attributed to I($^2P_{3/2}$) production with counterfragments of both ground state O_2 ($^3\Sigma_g^-$) the first electronically excited state O_2 ($^1\Delta_g$). To be sure the lower translational energy portion of the distribution is not due to photoionization of I($^2P_{1/2}$), which is separated by 21.7 kcal/mol from I($^2P_{3/2}$), a TOF spectrum was taken with the visible laser for the second REMPI step blocked. Under these conditions, no I^+ signal was observed, indicating no contribution from I($^2P_{1/2}$). In addition to the two electronic states of O_2, the P(E) shows the O_2 counterfragments are generated with a distribution of vibrational states, with significant populations beyond v = 6. By using separate P(E)'s for contributions corresponding to O_2 ($^3\Sigma_g^-$) and O_2 ($^1\Delta_g$), a branching ratio of 55% for O_2 ($^3\Sigma_g^-$) and 45% O_2 ($^1\Delta_g$) was determined. A significant population of O_2 ($^1\Delta_g$) has previously been predicted based upon calculations indicating the importance of the A^2B_2 state of OIO, which correlates to I($^2P_{3/2}$) + O_2 ($^1\Delta_g$).[28]

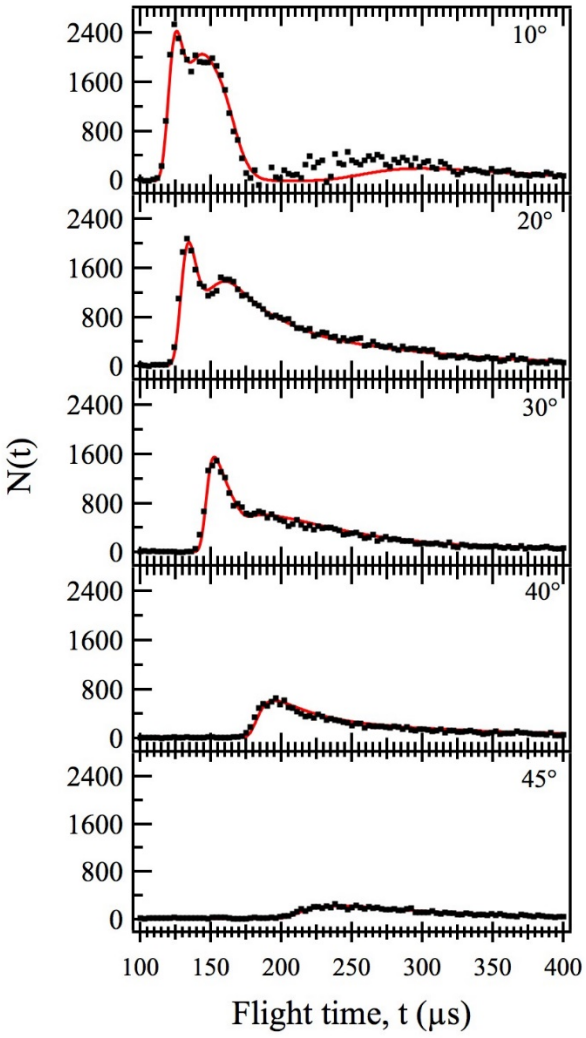

Figure 3.5: I($^2P_{3/2}$) TOF at indicated angles for 568 nm photodissociation. Black squares are experimental data, red solid lines are forward convolutions calculations using P(E) from Figure 3.6.

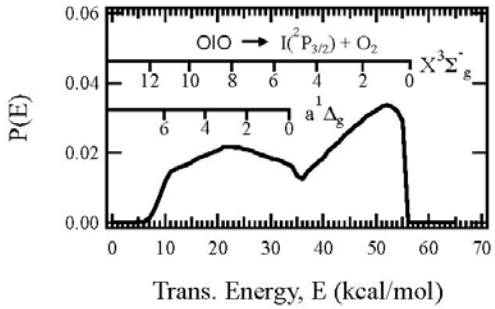

Figure 3.6: Photofragment translational energy distribution for OIO + hν (568 nm) → I($^2P_{3/2}$) + O_2.

The OIO absorption spectrum is highly structured with very strong peak absorption cross sections, reaching $1x10^{-17}$ cm^2 $molecule^{-1}$.[20,26] By scanning the photodissociation laser wavelength from 560 nm to 575 nm and monitoring the $I(^2P_{3/2})$ products at a laboratory angle of 20 degrees and a TOF arrival time of 135 μs, we recorded action spectra for $OIO \rightarrow I(^2P_{3/2}) + O_2$. The bandwidth of the dye laser is ~0.15 cm^{-1}, which is about 20 times smaller than the 0.10 nm step size. As illustrated in Figure 3.7, the action spectra were in very close agreement with the known OIO absorption spectra. As anticipated for jet cooled OIO samples, the absorption peaks were found to be much narrower than the published room temperature spectra, owing to the low rotational temperatures of molecules in the molecular beam.[20,26]

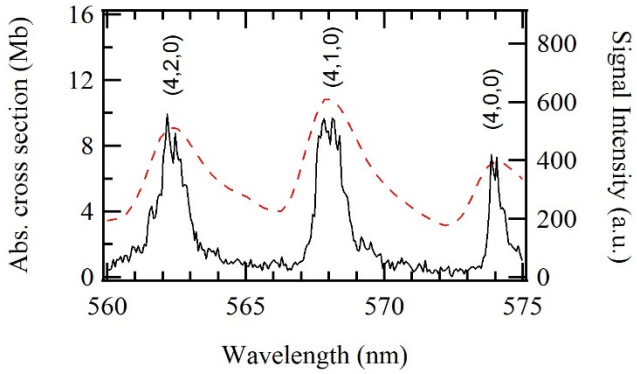

Figure 3.7: $I(^2P_{3/2})$ photofragment signal observed from 560-575 nm (black solid line) compared to the absorption spectrum from Ref. 20 (red dashed line). The wavelength was scanned with a step size of 0.10 nm.

C. 532 nm

Photodissociation of OIO was also studied at 532 nm, close to the (6,1,0) absorption peak of OIO. Figure 3.8 shows I($^2P_{3/2}$) TOF spectra for various lab angles. At this wavelength, signal from I_2 photodissociation can be seen in the TOF spectra due to greater relative absorption cross section for I_2 compared to OIO compared to the other wavelengths studied. In this case, I_2 photodissociation from the first ~6 vibrational levels leading to two I($^2P_{3/2}$) atoms was accounted for by factoring in an additional P(E) shown in Figure 3.9b, using the known dissociation energy (35.5 kcal/mol) and anisotropy parameter ($\beta = -1$) of I_2 at 532 nm.[32] The best-fit I + O_2 P(E) distribution, shown in Figure 3.9a, shows the maximum translational energy of the products to be 58 ± 2 kcal/mol, i.e. an energy change of -4.3 ± 2 kcal/mol for OIO → I ($^2P_{3/2}$) + O_2, 1 kcal/mol greater than the theoretical value.[28] Using two separate P(E) distributions for the two electronic states of O_2, it was estimated that the branching ratio of the oxygen molecules formed is 55% O_2 ($^3\Sigma_g^-$) and 45% O_2 ($^1\Delta_g$).

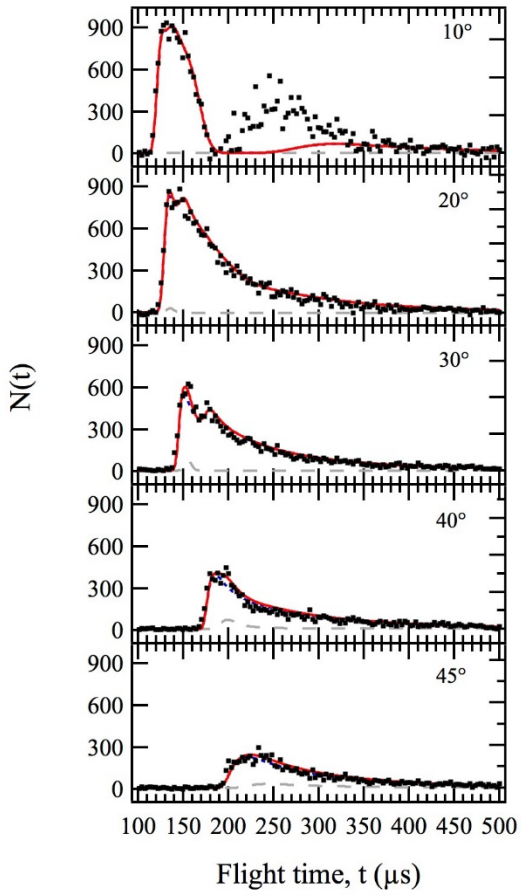

Figure 3.8: I($^2P_{3/2}$) TOF at indicated angles for 532 nm photodissociation. Black squares are experimental data. The red solid line is overall I signal forward convolution, the blue dotted line is contribution from OIO dissociation, and the grey dashed line is contribution from I_2 dissociation.

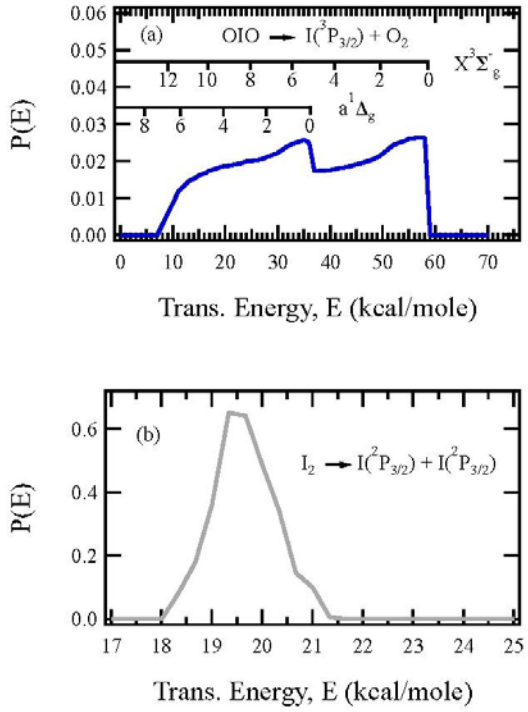

Figure 3.9: P(E) distributions for (a) OIO + hν (532 nm) →$I(^2P_{3/2})$ + O_2, and (b) I_2 + hν (532 nm) → $2I(^2P_{3/2})$.

D. 486 nm

Gómez Martín and Plane previously determined the wavelength threshold for the OIO → O + IO channel to be 480 ± 2 nm.[27] Figure 3.10 shows TOFs for $I(^2P_{3/2})$ at various lab angles for photodissociation at the (9,1,0) upper state at 486 nm, fit with the P(E) distribution shown in Figure 3.11a. Signal from I_2 photodissociation is accounted for using the P(E) distributions in Figure 3.11b and 3.11c, for dissociation to $I(^2P_{3/2})$ with counterfragments of $I(^2P_{3/2})$ and $I(^2P_{1/2})$ respectively, both of which are known to be

strongly anisotropic.[33] At this photodissociation energy, the branching ratio was again measured to be 55% O_2 ($^3\Sigma_g^-$) and 45% O_2 ($^1\Delta_g$). At this wavelength, the maximum translational energy is 63 ± 2 kcal/mol. Thus the OIO bond dissociation energy is measured to be -4.2 ± 2 kcal/mol, in good agreement with the values found at other wavelengths.

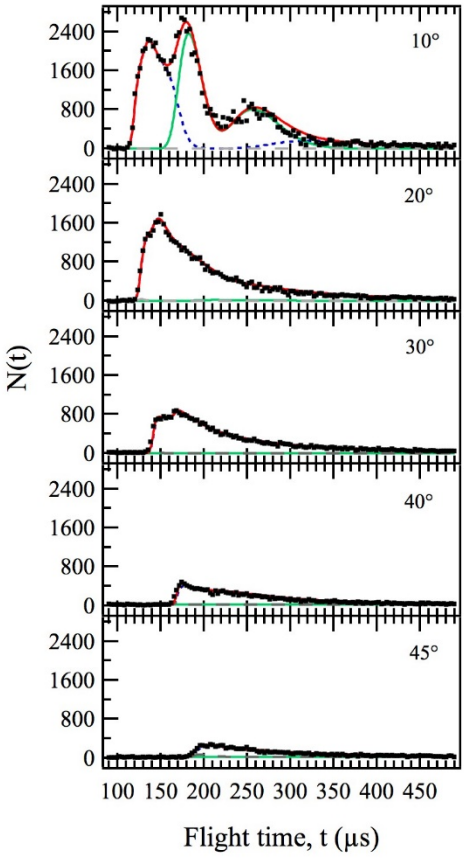

Figure 3.10: I($^2P_{3/2}$) TOF spectra at indicated angles from 486 nm photodissociation. Black squares are experimental data, red lines are total forward convolution. Blue dotted lines are from I + O_2. For I_2 dissociation, green solid lines are for a counterfragment of I($^2P_{1/2}$) and grey dashed lines are for a counterfragment of I($^2P_{3/2}$).

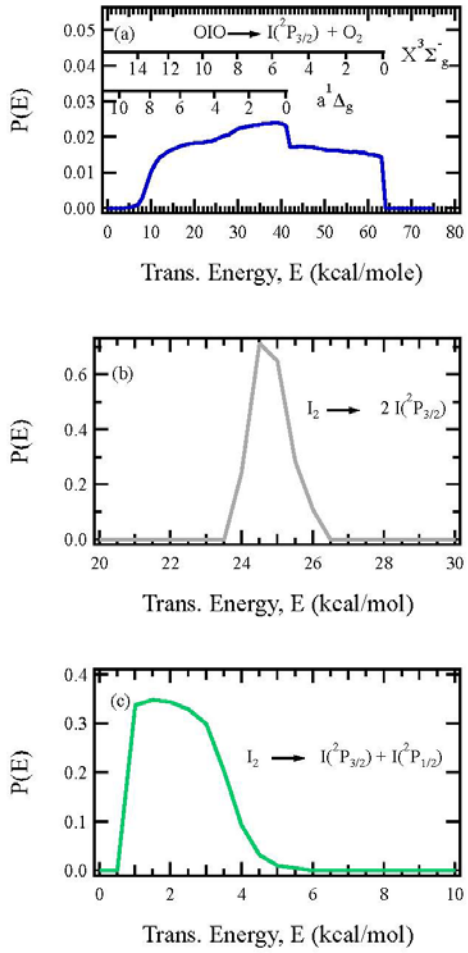

Figure 3.11: Photofragment translational energy distribution for a) OIO + hν (486 nm) → $I(^2P_{3/2}) + O_2$, b) I_2 + hν (486 nm) → 2 $I(^2P_{3/2})$, c) I_2 + hν (486 nm) → $I(^2P_{3/2}) + I(^2P_{1/2})$.

We observed fragmentation to I + O_2 at photodissociation wavelengths in the 465-495 nm range, with peaks matching the absorption spectrum recorded by Speitz *et al.*,[20] shown in Figure 3.12. The time-of-flight spectra for photodissociation at 473 nm were noisy due to small absorption cross section compared to the other wavelengths studied. However, the data can be fit suitably with a P(E) distribution similar to that at 486 nm, but

shifted to ~1.5 kcal/mol greater translational energy. Observation of the I + O_2 channel at this wavelength shows that the I+ O_2 channel is operative even at wavelengths shorter than the 480 nm threshold reported by Gómez Martín and Plane.

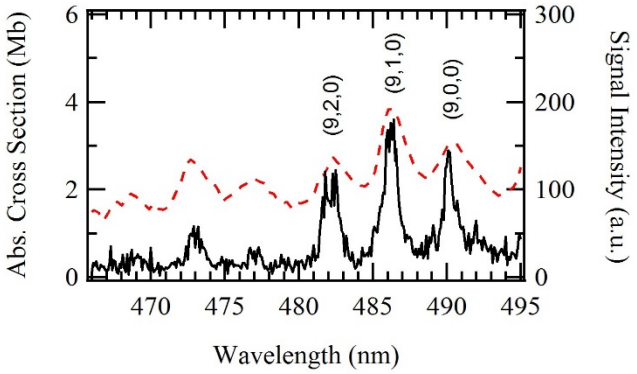

Figure 3.12: I($^2P_{3/2}$) photofragment signal observed from 465-495 nm (black solid line) compared to the absorption spectrum from Ref. 20 (red dashed line). The wavelength was scanned with a step size of 0.10 nm.

E. 634 nm

The TOF spectra recorded from the (1,1,0) upper state at 634 nm and the determined P(E) distributions are shown in Figures 3.13 and 3.14 respectively. Similar to the experiments at shorter wavelengths discussed above, contributions from both O_2 ($^1\Delta_g$) and O_2 ($^3\Sigma_g^-$) are present, and the dissociation energy is measured to be -4.0 ±2 kcal/mole. At this wavelength the P(E) distributions show approximately 55% of the O_2 photofragments being generated in the ($^1\Delta_g$) excited state. Photodissociation was observed at wavelength from 615 – 645 nm, with peaks corresponding to the absorption spectrum from Speitz *et al.*[20] as seen in Figure 3.15.

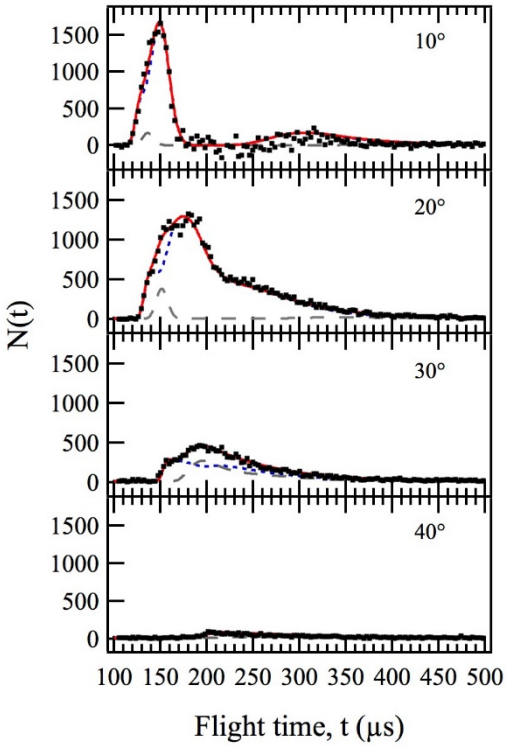

Figure 3.13: I($^2P_{3/2}$) TOF at indicated angles for 634 nm photodissociation. Black squares are experimental data. The red solid line is overall I signal forward convolution, the blue dotted line is contribution from OIO dissociation, and the grey dashed line is contribution from I_2 dissociation.

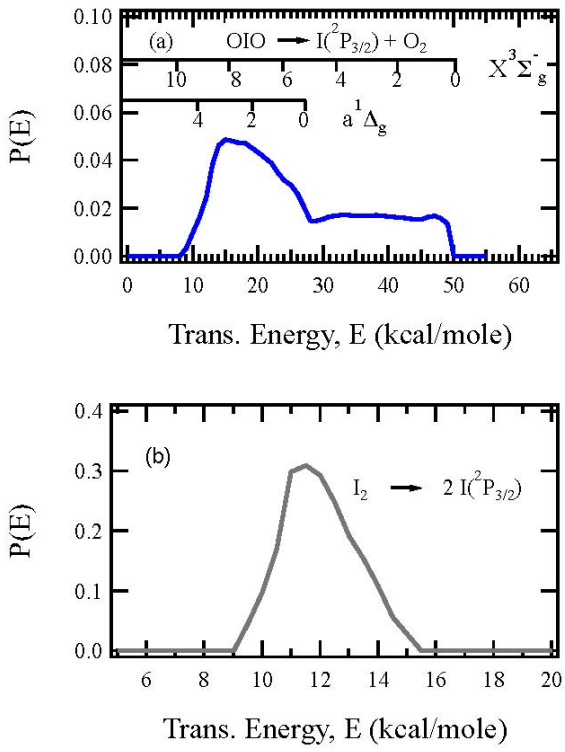

Figure 3.14: Photofragment translational energy distribution for a) OIO + hν (634 nm) → $I(^2P_{3/2}) + O_2$, and b) I_2 + hν (634 nm) → 2 $I(^2P_{3/2})$.

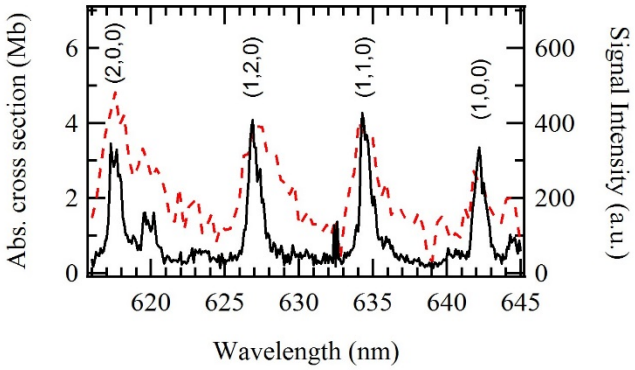

Figure 3.15: $I(^2P_{3/2})$ photofragment signal observed from 615-645 nm (black solid line) compared to the absorption spectrum from Ref. 20 (red dashed line). The wavelength was scanned with a step size of 0.10 nm.

At the shorter wavelengths, between 486 nm and 568 nm, we observed a consistent branching of 55% O_2 ($^3\Sigma_g^-$) and 45% O_2 ($^1\Delta_g$). In contrast, at the lowest photodissociation energy studied, 634 nm, the fraction of O_2 ($^1\Delta_g$) was 55%. As discussed above, dissociation to I + O_2 following excitation to the C $^2A_2$ state is believed to occur via spin-orbit coupling to the B^2A_1 state, followed by coupling to the A^2B_2 state through vibronic interactions at the avoided crossing between the two states. The A $^2B_2$ state has been calculated to have a relatively low barrier to I + O_2 ($^1\Delta_g$) dissociation compared to the C^2A_2 and B^2A_1 states, which correlate to I + O_2 ($^3\Sigma_g^-$).[28] In this long wavelength range, the large yield of O_2 ($^1\Delta_g$) could be evidence for involvement of the A^2B_2 state. The observation of a different trend in branching ratio between O_2 ($^1\Delta_g$) and O_2 ($^3\Sigma_g^-$) at shorter wavelengths might be evidence for involvement of a different mechanism. For example, at higher energies it is possible that I + O_2 is produced directly from the prepared C^2A_2 state, or alternatively, from the intermediate B^2A_1 state, without involvement of the low-lying A^2B_2 state.

F. Recoil anisotropy parameter

At 532 nm and 568 nm, laser polarization studies were carried out to determine the product angular distribution, I(θ). The product angular distribution from photodissociation of a linear molecule using a linearly polarized laser is given by: $I(\theta) = 1 + 2\beta P_2(\cos\theta)$, where θ is the laboratory angle relative to the polarization angle of the laser, P_2 is the second Legendre polynomial in cos(θ), and β is the anisotropy parameter which ranges from -1 to 2, with -1 corresponding to a perpendicular transition ($\Delta\Omega = 1$) and 2 corresponding to a parallel transition ($\Delta\Omega = 0$). A value of $\beta = 0$ corresponds to an isotropic product angular distribution.

The measurement was carried out by collecting TOF spectra at a given lab angle and at various polarization angles of the photodissociation laser relative to the detector axis. We observed no noticeable change in the TOF spectra with changing polarization angle, i.e. $\beta \approx 0$, corresponding to an isotropic product angular distribution. There are two possible explanations for anisotropy parameters differing from 2 or -1: 1) the dissociation lifetime exceeds its picosecond rotational period, or 2) dissociation occurs from nonlinear molecular geometries. In the latter case, β is reduced due to the nonzero angle between the angle of the transition dipole moment and recoil vector of the departing atom, as discussed in detail by Busch and Wilson.[34] For the specific case where the angle between the recoil vector and transition dipole moment is 54.5 degrees, $\beta = 0$ even in the limit of fast dissociation. For OIO, which is calculated to have a 100° equilibrium bond angle in the C^2A_2 excited state,[28] both factors are likely contribute to the isotropic distribution observed.

IV. Conclusions

We have studied the OIO $\rightarrow$ I + O_2 photodissociation channel at a number of different wavelengths. A wavelength dependent branching ratio between the ground O_2 ($^3\Sigma_g^-$) and excited O_2 ($^1\Delta_g$) channels was observed. In the wavelength range observed, higher photon energy led to a larger fraction of ground state O_2 ($^3\Sigma_g^-$). Also, from the maximum translational energy release, we have experimentally determined the OIO $\rightarrow$ I + O_2 reaction to be exoergic by 4.3 ± 2 kcal/mol.[28]

A number of questions still remain, including the branching ratio between the competing I + O_2 and O + IO channels at excitation energies above Do(O-IO). Since previous experiments have shown that fluorescence is absent following visible excitation

of OIO, we conclude that the quantum yield for I + O_2 production at $\lambda > 480$ nm must unity, in good agreement with the conclusions of Gómez Martín *et al.*[21] To date, we have not attempted to detect formation of electronically excited I($^2P_{1/2}$). Since it is well-known that I-O_2 electronic energy transfer is efficient, it would not be at all surprising if this channel plays an important role.

The value for the dissociation energy leading to ground state I and O_2 reported here assumes excitation of OIO originates from the X^2A_2 (0,0,0) level, with no contributions from hotband activity. Himmelman, *et al.*[19] did observe small absorption peaks ~70 cm^{-1} on the low energy side of strong absorption peaks (~2.3 nm at 568 nm), attributed to excitation from OIO ground electronic state molecules with v_2 bending excitation. Since no peaks attributable to hotband absorption were observed in our action spectra, we believe that our OIO beam is vibrationally cold. This supports the assumption that the OIO is initially in the X(0,0,0) ground state. However, if OIO in the molecular beam was initially internally excited, the maximum translational energy observed would not correspond to the minimum dissociation energy, but to dissociation from the vibrationally excited molecules in the molecular beam, i.e. $E_{int, OIO}$ cannot be assumed to be zero.

Mode specific photodissociation dynamics have been demonstrated in OClO,[35] Similar studies of OIO photodissociation are possible, investigating photodissociation from adjacent absorption peaks arising from different (v'_1, v'_2, v'_3) upper states.

V. References

1. M.B. McElroy, R.J. Salawitch, S.C. Wofsy, and J.A. Logan, *Nature* **321**, 795 (1986).

2. R.P. Wayne, G. Poulet, P. Biggs, J.P. Burrows, R.A. Cox., P.J. Crutzen, G.D. Hayman, M.E. Jenkin, G. LeBras, G.K. Moortgat, U. Platt and R. N. Schindler, *Atmos. Envir*. **29**, 2677 (1995).

3. R.J. Salawitch, S.C. Wofsy, E.W. Gottlieb, L.R. Lait, P.A. Newman, M.R. Schoeberl, M. Loewenstein, J.R. Podolske, S.E. Strahan, M.H. Proffitt, C.R. Webster, R.D. May, D.W. Fahey, D. Baumgardner, J.E. Dye, J. C. Wilson, K.K. Kelly, J.W. Elkins, K.R. Chan, and J.G. Anderson, *Science* **261**, 1146 (1993).

4. H. Canty, E.D. Rivie`re, R.J. Salawitch, G. Berthet, J.-B. Renard, K. Pfeilsticker, M. Dorf, A. Butz, H. Bösch, R.M. Stimpfle, D. M. Wilmouth, E.C. Richard, D. W. Fahey, P.J. Popp, M.R. Schoeberl, L.R. Lait, and T.P. Bui, *J. Geophys. Res.* **110**, D01301 (2005).

5. S. Solomon, R.W. Sanders, and H.L. Miller, Jr., *J. Geophys. Res.* **95**, 13807 (1990).

6. J.S. Daniel, S. Solomon, R.W. Portmann, and R.R. Garcia, *J. Geophys. Res.* **104**, 23871 (1999).

7. R. Schofield, P. V. Johnston, A. Thomas, K. Kreher, B. J. Connor, S. Wood, D. Shooter, M. P. Chipperfield, A. Richter, R. von Glasow, and C. D. Rodgers, *J. Geophys. Res.* **111**, D22310 (2006).

8. K.A. Peterson, B.C. Shepler, D. Figgen, and H. Stoll, *J. Phys. Chem. A.* **110**, 13877 (2006).

9. H.F. Davis and Y.T. Lee, *J. Phys. Chem.* **100**, 30 (1996).

10. H. Kim, J. Park, T.C. Niday, and S.W. North, *J. Chem. Phys.* **123**, 174303 (2005).

11. S. Schmidt, Th. Benter and R.N. Schindler, *Chem. Phys. Lett.* **282**, 292 (1998).

12. P. Zou, H. Kim, and S.W. North, *J. Chem. Phys*. **116**, 4176 (2002).

13. K.S. Dooley, J.N. Geidosch, S.W. North, *Chem. Phys. Lett.* **457**, 303 (2008).

14. B. Alicke, K. Hebestreit, J. Stutz, and U. Platt, *Nature* **397**, 572 (1999).

15. W.J. Bloss, D.M. Rowley, R.A. Cox, and R.L. Jones, *J. Phys. Chem. A* **105**, 7840 (2001).

16. D.M. Rowley, W.J. Bloss, R.A. Cox, and R.L. Jones, *J. Chem. Phys. A* **105**, 7855 (2001).

17. Y. Bedjanian, G. Le Bras, and G. Poulet, *J. Phys. Chem. A* **101**, 4088 (1997).

18. A.A. Turnipseed, M.K. Gilles, J.B. Burkholder, and A. R. Ravishankara, *J. Phys. Chem. A* **101**, 5517 (1997).

19. S. Himmelmann, J. Orphal, H. Bovensmann, A. Richter, A. Ladstgtter-Weissenmayer, J.P. Burrows, *Chem. Phys. Lett.* **251**, 330 (1996).

20. P. Spietz, J.C. Gómez Martín, J.P. Burrows, *J. Photochem. Photobiol. A* **176**, 50 (2005).

21. J.C. Gómez Martín, S.H. Ashworth, A. S. Mahajan, and J.M.C. Plane, *Geophys. Res. Lett.* **36**, L09802 (2009).

22. M.E. Tucceri, D. Holscher, A. Rodriguez, T.J. Dillon, and J.N. Crowley, *Phys. Chem. Chem. Phys.* **8**, 834 (2006).

23. T. Ingham, M. Cameron, and J.N. Crowley, *J. Phys. Chem. A* **104**, 8001 (2000).

24. D.M. Joseph, S.H. Ashworth, and J.M.C. Plane, *J. Photochem. Photobiol., A* **176**, 68 (2005).

25. R.A. Cox, W.J. Bloss, R.L. Jones, and D.M. Rowley, *Geophys. Res. Lett.* **26**, 1857 (1999).

26. S.H. Ashworth, B.J. Allan, and J.M.C. Plane. *Geophys Res. Lett.* **29**, 1456 (2002).

27. J.C. Gómez Martín and J.M.C. Plane, *Chem. Phys. Lett.* **474**, 79 (2009).

28. K.A. Peterson, *Mol. Phys.* **108**, 393 (2010).

29. R. Sommariva, W. J. Bloss and R. von Glasow, *Atmos. Environ.* **57**, 219 (2012).

30. P.A. Willis, H.U. Stauffer, R.Z. Hinrichs, and H.F. Davis, *Rev. Sci. Instrum.* **70**, 2606 (1999).

31. D.R. Albert, D.L. Proctor, and H.F. Davis, *Rev. Sci. Instrum.* **84**, 063104 (2013).

32. C.-L. Liu, H.-C. Hsu, and C-K. Ni, *Phys. Chem. Chem. Phys.* **7**, 2151 (2005).

33. D.A. Chestakov, D.H. Parker, K.V. Vidma, and T.P. Rakitzis, *J. Chem. Phys.* **124**, 024315 (2006).

34. G.E. Busch and K.R. Wilson, *J. Chem. Phys.* **56**, 3638 (1972).

35. H.F. Davis and Y.T. Lee, *J. Chem. Phys.* **105**, 8142 (1996).

CHAPTER 4

COMPETITION BETWEEN I AND HI PRODUCTION FROM IODOPROPANE PHOTOLYSIS AT 266 NM

I. Introduction

The ultraviolet photodissociation of alkyl iodides has been an active area of study over many decades. This class of molecules has served as benchmarks for comparing theoretical calculations to experimental results, investigating the crossings between various electronic states and their impact on the photodissociation dynamics. Alkyl iodide photodissociation also represents simple test systems for the development of new experimental techniques. Photodissociation experiments on alkyl iodides have also provided insight into the effects alkyl radical size, isomeric form, and the effect of substitutions (i.e. CH_3 vs. CF_3).

1-iodopropane and 2-iodopropane represent the simplest systems where the photodissociation dynamics of two different iodoalkane isomers can be compared directly. By analogy to methyl iodide, two different atomic iodine elimination channels, leading to formation of ground I($^2P_{3/2}$) or the spin-orbit-excited state I($^2P_{1/2}$) (hereafter referred to as I and I*, respectively) are observed.[1,2,3,4,5,6,7,8,9] Whereas many studies of the I and I* channels have been published for photodissociation of iodoalkanes containing more than one carbon atom, only one 1999 report, by Ross and Johnston,[10] considered the HI elimination channel. While HI was clearly observed for branched iodoalkanes in that work, the branching ratios, kinetic energy distributions, and product angular distributions were not investigated. As in the case of methyl iodide, initial excitation of propyl iodide leads to

the $^3Q_0$ excited state correlated with I* products. Non-adiabatic crossing to the $^1Q_1$ excited state leads to formation of ground state I.

The thermal decomposition of alkyl iodides is known to lead to competition between simple C-I bond fission, forming alkyl radicals, and HI elimination producing alkenes, with the latter channel becoming more important for more highly branched species. From these studies,[11] activation energies have been derived for the I and HI elimination channels on the ground alkyl iodide electronic states. In this work, we present the first experimental studies of HI elimination from iodoalkane photodissociation using photofragment translational energy spectroscopy:

$$2\text{-}C_3H_7I + h\nu\ (266\ nm) \rightarrow C_3H_7 + I(^2P_{3/2}) \quad \Delta H = 52.95\ kcal/mol \quad (1a)$$

$$\rightarrow C_3H_6 + HI \quad \Delta H = 20.62\ kcal/mol \quad (1b)$$

By measuring the product angular and velocity distributions, insight into the dissociation mechanisms is obtained. In the present work, products are detected under identical conditions using two complementary methods, *i.e.*, electron impact ionization, and photoionization. The availability of two complementary detection methods provides a valuable cross check of the branching ratios derived for the competing reaction pathways.

II. Experimental

The experiments were carried at Cornell University out using a rotatable source crossed molecular beams apparatus equipped with both VUV photoionization and electron impact ionization detection, discussed in Chapter 1.[12] Vacuum ultraviolet light was produced via four-wave sum-frequency mixing of unfocused dye lasers (produced by two separate Lambda-Physik Scanmate 2 dye lasers pumped by a common injection-seeded

Powerlite 9030 Nd:YAG laser) in a long heated Hg cell, as described previously.[13] In all experiments, the two-photon 7S resonance in Hg at 312.85 nm was used. The 312.85 nm light was produced by mixing in a BBO crystal the 759 nm light from the dye laser with the 532 nm light from an injection-seeded Nd:YAG laser. The second color (625-728 nm) employed in the four wave mixing process was produced in the second dye laser. The ground state I($^2P_{3/2}$) products were selectively ionized by two-color excitation through the $5s^25p^4(^3P_2)8s\ ^2[2]_{3/2}$ state at 128.94 nm. The second photon for ionization was residual 312.85 or 733.8 nm laser radiation (produced by a second dye laser for VUV generation). Detection of I*, HI, C_3H_7, and C_3H_6 fragments employed single photon ionization near 9.9 eV (second dye laser near 625 nm) or 11.9 eV (third harmonic of 312.85 nm generated using one dye laser). Since the ionization energy of HI is 10.38 eV[14], only vibrationally excited HI ($v > 3$) can be ionized at 9.9 eV.[10] As discussed below, the P(E) distributions for the HI products were found to be the same using 9.9 eV, 11.9 eV, and electron impact ionization, demonstrating that essentially all HI products are in $v > 3$.

The apparatus employs a windowless VUV beamline, facilitating efficient access to wavelengths near the LiF transmission cutoff at 104.4 nm. For the experiments described here, two unfocussed laser beams (e.g., 312.55 and 625 nm) were combined in a 0.5 m high pressure (~15 Torr Hg and 50 Torr He) heat pipe (130^{o}C). The VUV generated by resonance-enhanced four-wave sum mixing then propagated through an 18'' long, 1/8'' I.D. stainless steel tube followed by three stages of differential pumping. Using this arrangement, the ionization region of the detector can be maintained below 1×10^{-9} Torr during the experiment. The present method provides the option of generating high intensity VUV radiation at energies as high as 11.9 eV ($\lambda = 104.4$ nm).[13] For $\lambda > 110$ nm, the VUV

and can be dispersed from the fundamental beams by passage through a pair of MgF_2 optics. The first optic is a 0.25" thick flat window held at Brewster's angle (to minimize reflection losses) mounted on a vacuum manipulator, allowing it to be inserted into the beam to laterally deviate the beam off of but parallel to its original axis. The second optic, a 50 cm FL MgF_2 lens is mounted on a separate translation stage. By adjusting the lens so that the laser passes slightly away from its center, the VUV beam is directed into the ionization region of the detector. Owing to their smaller indices of refraction, the UV and visible beams are deflected less by the second optic and are spatially separated from the VUV beam. For production of 11.9 eV light (104.3 nm), the third harmonic of the 312.85 nm laser was produced by loosely focusing the UV beam into the cell using a 1 m FL lens. Although in an earlier configuration the VUV was spatially separated from the residual 312.85 nm light by reflection off one or two antireflection windows (AR coated at 312.85 nm), in the present work a collinear optical arrangement was used without removing the residual 312.85 nm beam.

The differentially pumped molecular beam source can be rotated relative to the fixed mass spectrometer detector consisting of a photoionization region, quadrupole mass filter, and ion detector. Samples of 1-iodopropane (Aldrich 99.9%, held at 18°C) and 2-iodopopane (Aldrich 99.9%, 0°C) were used without further purification. The molecular beams were generated by piezoelectrically actuated pulsed values, seeded with He at a total backing pressures of ~1000 Torr. The 266 nm light produced by an unseeded (1 cm^{-1} bandwidth, Continuum 9030 Nd:YAG laser) intersected the molecular beam along the axis of rotation. A fraction of photodissociation products drift a fixed distance from the main chamber ($P < 10^{-6}$ Torr during experiment) through three regions of differential pumping

to the ionization region of the UHV detector. For photoionization experiments (flight distance 15 cm), product time-of-flight (TOF) spectra were obtained by scanning the delay of the photoionization laser with respect to the photolysis laser using a digital delay generator (Stanford Research DG535). Detected ions for a given delay were integrated at each step using a gated photon counter (Stanford Research SR400). Signal was typically collected for one hundred laser shots at each delay step. For electron impact detection (flight distance = 30 cm), product TOF spectra were recorded using a SRS Multichannel Scaler (SR 400).

Through conservation of energy, the internal energy of the parent molecule and photon energy is related to the translational and internal energy of the photofragments:

$$E_{photon} + E_{int,C3H7I} = D_0(C_3H_6\text{-}HI) + E_{trans,HI+C3H7} + E_{int,HI} + E_{int,C3H6} \qquad (1)$$

Analyses of the product TOF distributions were carried out using a forward convolution program, taking the known parameters of the crossed beam apparatus and molecular beam, and user-generated product translational energy distributions, P(E), and anisotropy parameters, β, as inputs. Using these parameters as inputs, the program calculated TOF spectra for comparison to the experimental spectra. The P(E) and β parameters, as well as weighting factors for competing channels were iteratively adjusted until the calculated TOF spectra adequately simulated the experimental data.

III. Results and Discussion

A. 1-iodopropane

1. $I(^2P_{3/2})$

In Figure 4.1 the TOF spectra for $I(^2P_{3/2})$ from 1-C_3H_7I photodissociation using resonant photoionization are shown. The solid line represents the calculated TOF using the P(E) from Figure 4.2a and $\beta = 1.85$. We observed a most probable translational energy of 27 kcal/mole; thus 49% of available energy is distributed into internal excitation of the propyl radical. Previous measurements of 1-iodopropane photodissociation at this wavelength showed similar values.[6,15]

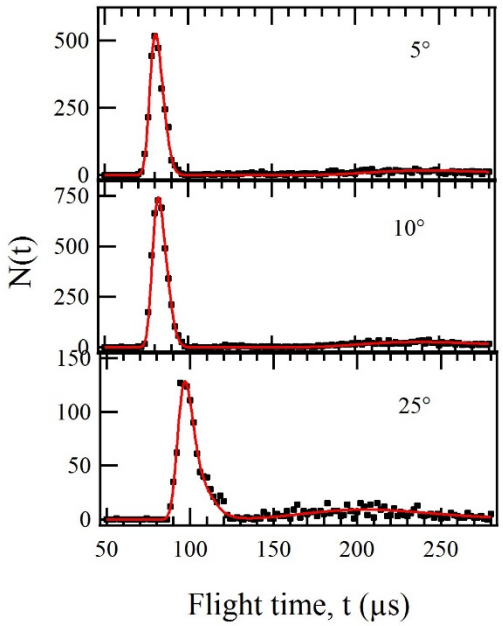

Figure 4.1: Time-of-flight spectra for $I(^2P_{3/2})$ at indicated lab angles. Black squares are experimental data, and red lines are best fits using P(E) shown in Figure 4.2a.

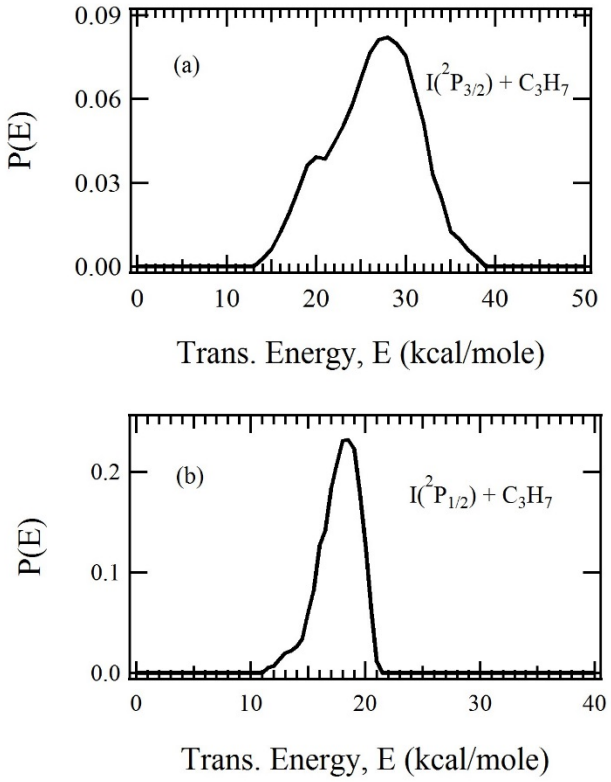

Figure 4.2: Translational energy distributions for a) I + 1-propyl, and b) I* +1- propyl photodissociation of 1-iodopropane at 266 nm.

2. $I(^2P_{1/2})$

Time-of-flight spectra for photodissociation of 1-iodopropane producing I* are shown in Figure 4.3, using the P(E) from Figure 4.2b. In these experiments, 9.9 eV nonresonant photoionization was used. The translational energy distribution showed a most probable translational energy of 18.5 kcal/mole, in good agreement with previous studies.

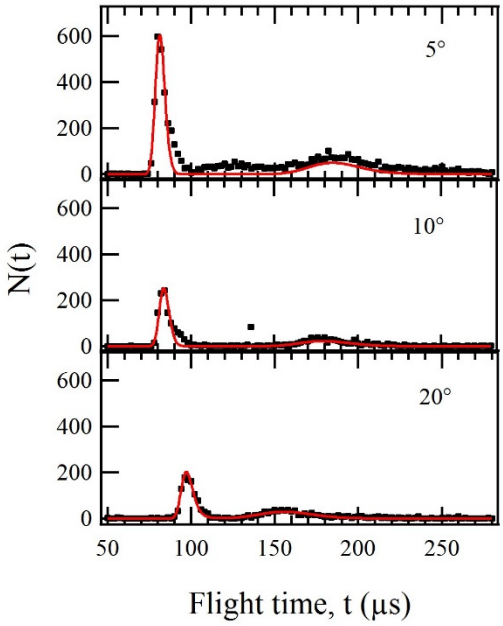

Figure 4.3: Time-of-flight spectra for I($^2P_{1/2}$) at indicated lab angles. Black square are experimental data, and red lines are forward convolution using P(E) shown in Figure 4.2b.

3. 1-C_3H_7

Time-of-flight spectra for propyl radicals (m/e = 43) from 1-iodopropane photodissociation (9.9 eV photoionization) are shown in Figure 4.4, using the same P(E) distributions used to simulate the I and I* channels (above). For photodissociation of 1-C_3H_7I, the arrival times for the propyl radicals correlating to the two different I atomic states are well-resolved. Assuming that the ionization efficiencies for propyl radicals correlated to the two different I atom states are the same, the weighting of the two P(E)s for the propyl data provides the I:I* branching ratio directly. As a cross-check, TOF data for m/e = 127 (I atoms) and m/e = 43 (C_3H_7) were obtained using 100 eV electron impact ionization. We also recorded TOF data using both electron impact ionization and photoionization at m/e = 42 ($C_3H_6^+$) in order to see whether or not the propyl ion

fragmentation pattern depends upon internal energy or if it differs for propyl radicals correlated to I and I*. No such dependence was observed. Using the electron impact ionization data, the C_3H_7 and I TOF spectra were also fit using the P(E) determined from photoionization experiments, again weighted to properly fit the experimental data. From photoionization of 1-C_3H_7, a I:I* branching ratio of 28:72 was determined, and from electron impact a ratio of 29:71 was obtained. The anisotropy parameter for the I* channel was found to be $\beta = 1.9$. This is slightly larger than obtained in previous measurements.

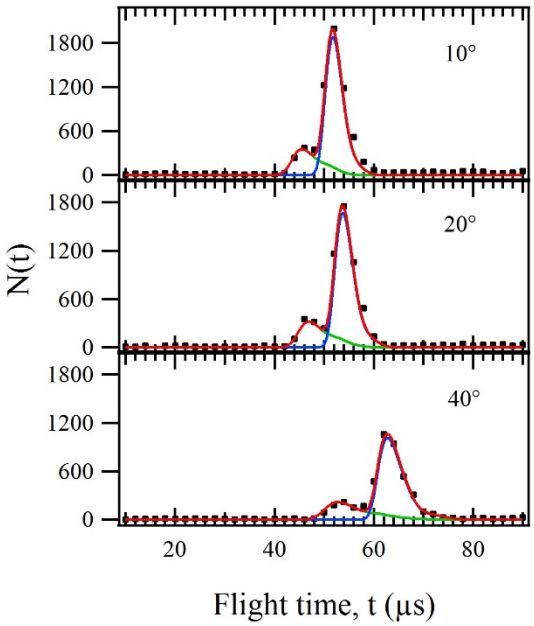

Figure 4.4: Time-of-flight spectra for 1-C_3H_7 at indicated lab angles. Black square are experimental data, red line is total forward convolution, green line is are contributions from I($^2P_{3/2}$), and blue is contribution from I*.

B. 2-iodopropane

1. $I(^2P_{3/2})$

Time-of-flight spectra for ground state I from photodissociation of 2-C_3H_7I are shown in Figure 4.5, fit with the P(E) distribution shown in Figure 4.6a. The most probable translational energy was measured to be 21 kcal/mole. This value, and the maximum translational energy of ~38 kcal/mole, are in reasonable agreement with those previously measured.[1,6,7,9]

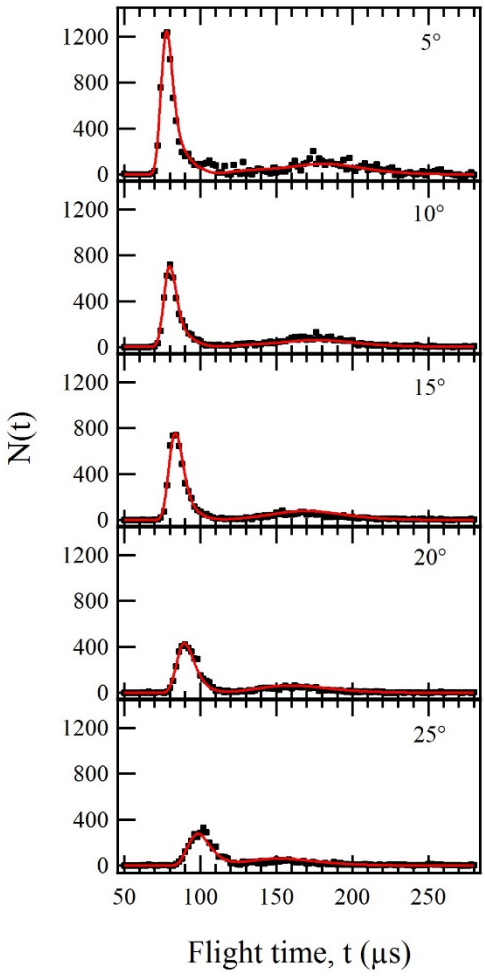

Figure 4.5: Time-of-flight spectra for $I(^2P_{3/2})$ photofragments from 2-iodopropane at given angles. Black square are experimental data, red lines are forward convolutions using the P(E) from Figure 4.6a.

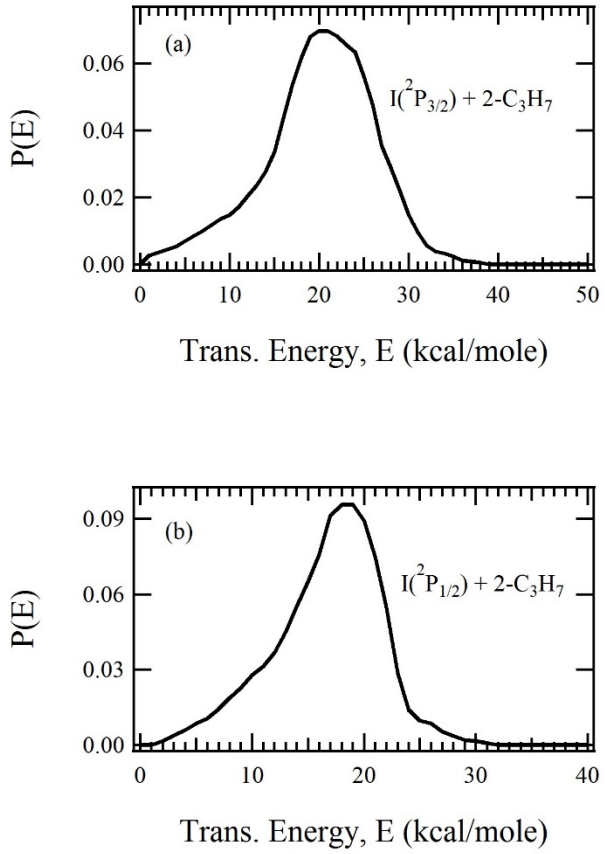

Figure 4.6: Translational energy distributions for I +2- propyl (top) and I* + 2-propyl (bottom) photodissociation of 2-iodopropane at 266 nm.

2. $I(^2P_{1/2})$

Nonresonant single photon ionization of I* was carried out using 9.9 eV light. Time-of-flight spectra for I* from photodissociation of 1-C_3H_7I are shown in Figure 4.7, fit with the P(E) distributions in Figure 4.6b. The most probable translational energy of this channel is 18 kcal/mole, with maximum observed translational energy of ~32 kcal/mole. Because the P(E) distributions for the I and I* translational energy distributions are similar for 2-C_3H_7I photodissociation, their contributions to the TOF spectra are overlapped. Therefore, the TOF spectra recorded using electron impact ionization provides only the net overall

kinetic energy distributions for both channels. In order to determine the I:I* branching ratio using photoionization detection, the relative detection sensitivity for I and I* is needed. Since we have determined the I:I* branching ratio for 1-iodopropane photodissociation independently, as described above, the I:I* detection sensitivity under our specific experimental conditions can be determined directly. Therefore, the I:I* branching ratio for 2-iodopropane can be obtained by running parallel experiments in which the I and I* signals from 1- and 2- iodopropane are detected back-to-back under identical experimental conditions. Using this approach, we found the branching ratio for I:I* for 266 nm photodissociation of 2-iodopropane to be 88:12. This sharply contrasts that for 1-iodopropane, where the branching ratio was found to be 28:72.

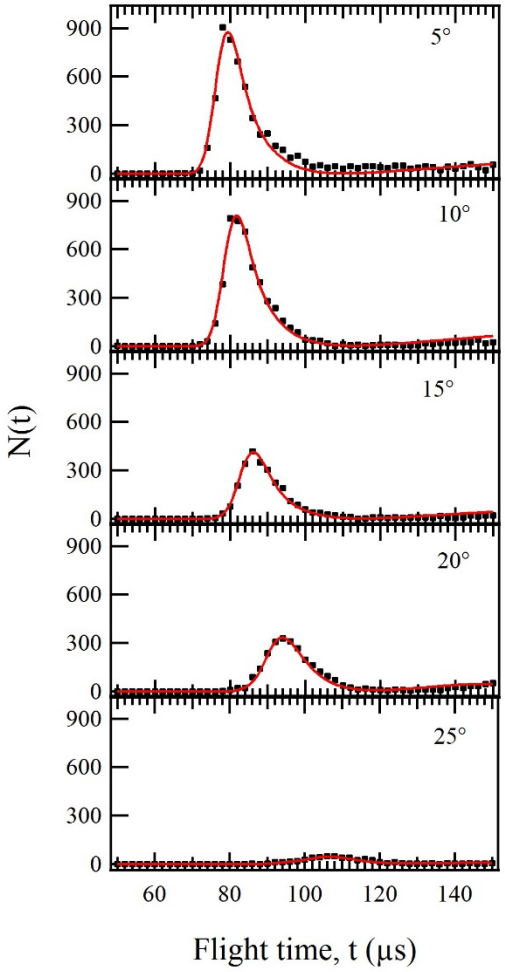

Figure 4.7: Time-of-flight spectra for I($^2P_{1/2}$) at indicated lab angles. Black square are experimental data, and red lines are forward convolution using P(E) shown in Figure 4.6b.

3. 2-C_3H_7

Detection of the propyl radicals from 2-iodopropane photodissociation was carried out with nonresonant photoionization at 9.9 eV. Fits using the P(E) distributions determined from I and I* detection were found to overestimate the fraction of radicals with low translational energy. Fan and Pratt reported similar behavior, and attributed it to greater fragmentation of vibrationally excited C_3H_7 upon photoionization.[6] Detection of 2-C_3H_7 radicals using electron impact ionization also indicated a dependence of the fragmentation

pattern on the translational energy. This behavior contrasts that seen for the propyl radicals from 1-iodopropane, where there was no detectible difference of the fragmentation pattern on internal excitation of the radicals.

4. HI elimination

Excitation at 266 nm populates mainly the $^3Q_0$ electronic state,[1,4,8] which dissociates to produce I*. Curve crossing to the lower $^1Q_1$ state leads to production of I. Alternatively, four-center HI elimination can occur, as demonstrated experimentally for both photodissociation in this work, and in the work by Ross,[10] and in previous studies of alkyl iodide thermal decomposition.[11] In the latter work, Miyoshi *et al*. discussed the differences in thermal dissociation branching pathways for primary, secondary, and tertiary bonded alkyl iodides. Thermal decomposition of 2-iodopropane at 1 atm and temperatures from 950-1100 K was shown to have an C-I bond fission branching fraction of ~35%, which is lower than the ~75% found for 1-iodopropane.[11] From this behavior, it was concluded that the potential energy barrier for HI elimination from secondary iodides on the ground state surface is ~3.3 kcal/mol lower than for primary iodides. It was suggested that the decrease in potential energy barrier is associated with the presence of secondary CH_3 groups adjacent to the C-I moiety. The potential energy barrier for HI elimination results from the avoided crossing between surfaces correlated to the $R^+ + I^-$ ionic dissociation surfaces and the repulsive potential energy surfaces correlated to HI + alkenes. As illustrated in Figure 4.8, the energies for the ionic dissociation surfaces decrease with increasing number of CH_3 substituents, leading to lower adiabatic barriers for HI elimination from secondary alkyl iodides relative to primary iodides. Similar interactions are likely to be present between the

HI + alkene repulsive surfaces and the electronically excited states of alkyl iodide molecules. This picture differs somewhat from a previous suggestion that the yield of HI elimination products from electronically excited alkyl iodides depends upon the *number* of secondary H atoms in the two isomers, which is 2 for 1-iodopropane and 6 for 2-iodopropane. The complete absence of HI elimination from 1-iodopropane indicated by our work suggests that the avoided crossing necessary to access the HI elimination channel is not accessible at 266 nm. Theoretical calculations on the excited states of alkyl iodides are necessary in order to better unravel the interesting isomer-specific photodissociation dynamics observed in this work. Also, a study of the wavelength dependence of the HI:I branching ratio using a tunable excitation source would be interesting.

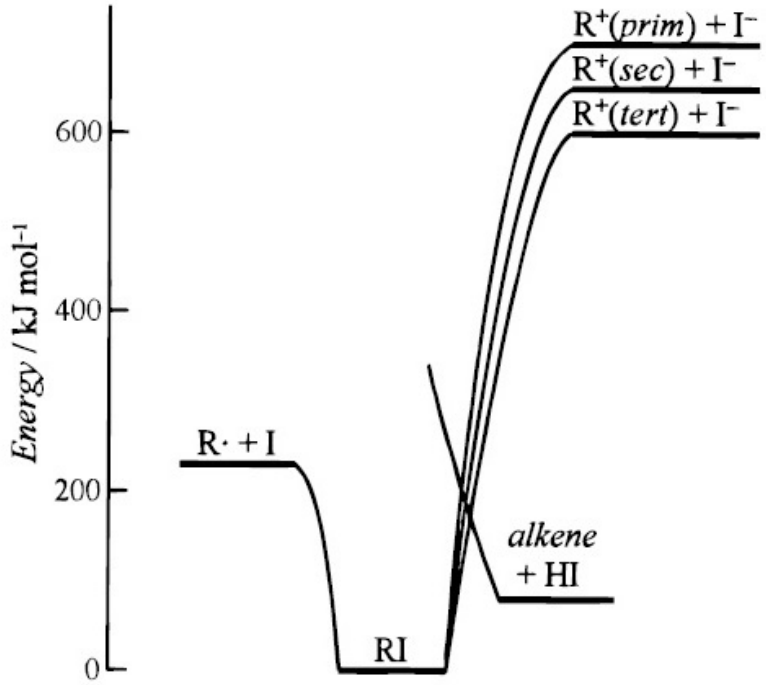

Figure 4.8: Interpretation for four-center HI elimination based on α-substituent effects on the avoided intersection with ionic dissociation surface, reproduced from Miyoshi et al., Figure 7.[11]

Figure 4.9 shows TOF spectra for vibrationally excited HI, detected at 9.9 eV. The maximum available translational energy, corresponding to formation of vibrational ground state HI and C_3H_6, is E_{avail} = 87 kcal/mol. From the P(E) distribution in Figure 4.10, the most probable translational energy is 22 kcal/mol, with the maximum observed translational energy of ~38 kcal/mol. Clearly, HI elimination occurs with a significant fraction of available energy distributed into the internal energy of the photofragments. As already noted, our experiments demonstrate that essentially all HI is produced in v > 3. In the absence of vibrationally-resolved HI photoionization, we are not able to provide further insight into the distribution of energy in the HI + C_3H_6 products.

In order to ensure that the signal attributed to HI elimination at m/e = 128 does not result from imperfect mass resolution, i.e., from spillover from I at m/e = 127, we studied the photodissociation of CF_3I at 266 nm. Since CF_3I dissociates to CF_3 + I and cannot lead to HI production, any signal observed at m/e = 128 in the CF_3I experiment must result from spillover from m/e = 127. Under our experimental conditions, spillover at m/e = 128 was found to be 1.1% using CF_3I using electron impact ionization. Using electron impact ionization detection, the signal levels observed for 2-iodopropane at m/e = 128 was about 10% of that observed at m/e = 127. Therefore, ~90% of the electron impact signal observed at m/e = 128 results from HI with only 10% resulting from I. As will be noted below, even after accounting for spillover, the TOF and polarization angular distributions for HI from 2-iodopropane photodissociation were very similar to that for I. For photoionization detection at 9.9 eV, the HI signal levels were comparable to that for I. In the CF_3I photodissociation experiments using 9.9 eV photoionization, spillover at m/e = 128 was

found to be < 3%. Therefore, the contribution to the HI signal at m/e = 128 from I spillover in the photoionization experiments was less than 3% and could be neglected.

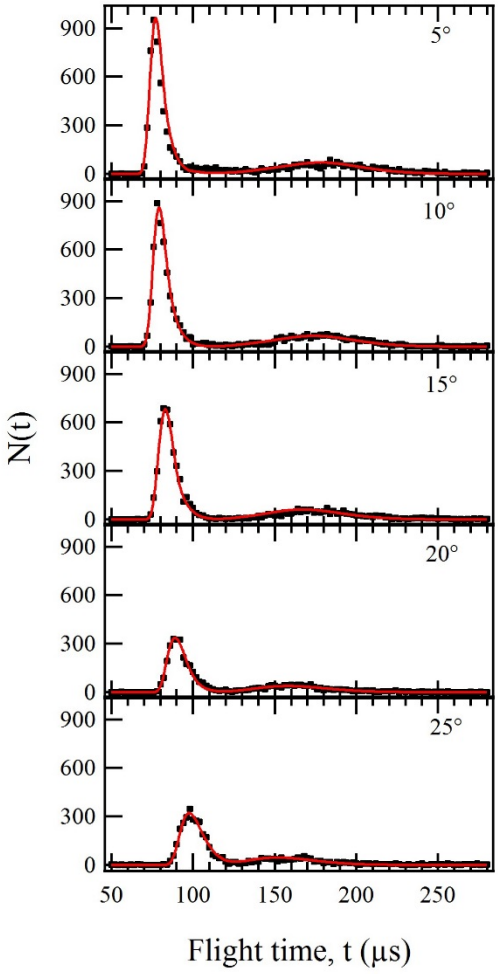

Figure 4.9: TOF spectra for HI elimination at given lab angles. Black square are experimental data, red lines are forward convolution using the P(E) shown in Figure 4.10.

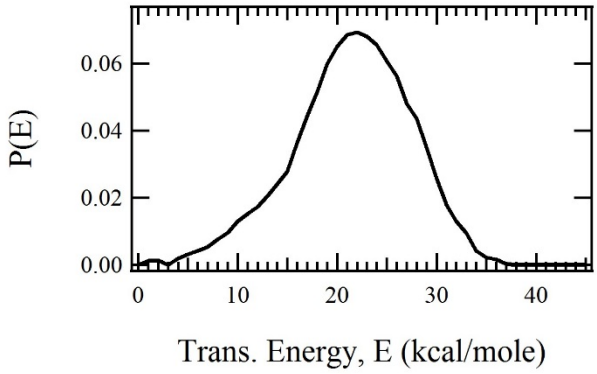

Figure 4.10: Translational energy distribution for HI elimination channel.

The anisotropy parameter for HI elimination was also measured. Similar to the I + propyl channels, HI elimination is strongly anisotropic, with $\beta \sim 1.7$. Thus, the anisotropy parameter for the HI elimination channel is only slightly smaller than that observed for the dominant ground state I channel.

Using electron impact ionization, the integrated signal levels from HI detection and I detection at a given angle are used to estimate the branching ratio between the two channels. Assuming the electron impact ionization cross sections are similar for I and HI (a reasonable assumption since ionization cross sections scale with molecular polarizability which are 34.6 au for I($^2P_{3/2}$), 35.1 au for I*, and 36.8 au for HI),[16,17] the HI elimination channel accounts for 9% of dissociation products at 266 nm.

C. Anisotropy Parameter

For each of the dissociation channels, experiments were carried out to determine the anisotropy parameters, β. This involved two measurements. First, for each detected species, at a given lab angle a $\lambda/2$ waveplate was used to rotate the linearly polarized 266 nm laser polarization to various angles relative to the detector axis, and TOF spectra were recorded.

Using the P(E) distributions determined above, β was adjusted to fit the TOF distributions at all detector angles. The second approach involves finding the polarization angle producing the minimum signal level for a given product channel at a selected laboratory angle. This angle was found by iteratively recording product TOF spectra at various polarizations. The ratio of the minimum signal level to the maximum (corresponding to a laser polarization 90° from the minimum) may be used to calculate β directly. Results of our measurements are summarized in Table 2, together with branching ratios and average translational energy values for each channel presented here. The anisotropy parameters determined here are closer to the limit for completely parallel transitions (β = 2) than reported in previous studies. The laboratory angular acceptance range of our detector is very narrow, only 1.5 degrees full width at half maximum. This, combined with the narrow range of beam velocities of the supersonic molecular beam, and the relatively narrow kinetic energy distributions, leads to a very narrow range of CM recoil angles detected at a given laboratory angle. Consequently, our experiment is very sensitive to β. After considering the various uncertainties associated with the measurement of β in our experiment, our derived values of β represent lower limits to the true value. Since our derived values are very close to the maximum limiting values of 2.0, the I and HI channels must occur on timescales that are much faster than that for molecular rotation, ~10^{-12}s.

Table 4.1: Dissociation energies (or Energy change), available energy, most probable translational energy, anisotropy parameter, and quantum yield for each channel studied for 1- and 2-iodopropane.

	Prod	D_0 (kcal/mol)	E_{avail} (kcal/mol)	‹E_{trans}› (kcal/mol)	‹E_{trans}›/ E_{avail}	β	ϕ(266 nm)
1-C_3H_7I	I	54.49	52.95	27	.51	1.85	.28
	I*	74.71	32.75	18.5	.56	1.9	.72
2-C_3H_7I	I	52.95	54.49	20	.37	1.8	.80
	I*	74.69	32.77	18	.55		.11
	HI	ΔH 20.62	86.84	22	.25	1.7	.09

IV. Conclusions

We have found that photodissociation of 2-iodopropane at 266 nm produces 9% vibrationally excited HI, with 25% of available energy appearing as translational energy. The remaining 75% of the available energy is distributed as internal excitation of the HI and propene, with essentially all of the HI produced in v > 3. Additionally, independently determined P(E) distributions and branching ratios for the I and I* channels from 266 nm photodissociation of both 1-iodopropane and 2-iodopropane are presented. For photodissociation of 1-iodopropane, as in the case of CH_3I, the I atom products are formed primarily in their spin orbit excited $^2P_{1/2}$ state. However, in the case of 2-iodopropane, the dominant I atom channel corresponds to production of ground state I $^2P_{3/2}$. For photodissociation of 2-iodopropane, the angular and velocity distributions for HI products were found to be very similar to those for I atoms. These observations clearly indicate that the H atom, with a mass 127 times smaller than I, acts essentially as a spectator in the HI

elimination dynamics. The slightly larger translational energy release for the HI channel (relative to the I channel) reflects the repulsive nature of the potential energy surface anticipated for the HI + alkene exit channel. Furthermore, from the large anisotropy parameter for HI production, this channel, like that for I production, must occur promptly likely without significant involvement of the alkyl iodide ground electronic state. The finding that HI elimination is significant for only 2-iodopropane suggests that the transition state for HI elimination is only accessible at 266 nm for the 2- isomer. Theoretical calculations on the potential energy surfaces for HI elimination and their interactions with the excited states of 1- and 2- iodopropane would facilitate a more quantitative understanding of the isomer-specific branching ratios observed in this study.

V. References

1. S.J. Riley and K.R. Wilson, *Faraday Discuss. Chem. Soc.*, **53**, 132 (1972).

2. P. Brewer, P. Das, G. Ondrey, and R. Bersohn, *J. Chem. Phys.* **79**, 720 (1983).

3. Q. Zhu, J.R. Cao, Y. Wen, J. Zhang, X. Zhong, Y. Huang, W. Fang, and X. Wu, *Chem. Phys. Lett.* **144**, 486 (1988).

4. S. Uma and P.K. Das, *Can. J. Chem.* **72**, 865 (1994).

5. S. Uma and P.K. Das, *J. Chem. Phys.* **104**, 4470 (1996).

6. H. Fan and S.T. Pratt, *J. Chem. Phys.* **123**, 204301 (2005).

7. X. Xu, Z. Yu, W. Bi, D. Xiao, D. Yu, Y. Du, and Q. Zhu, *J. Phys. Chem.* **112**, 1857 (2008).

8. K.-S. Lee, K. W. Lee, S. K. Lee, K.-H. Jung, T. K. Kim, *J. Mol. Spec.* **249**, 43 (2008).

9. V. A. Shubert, M. Rednic, and S. T. Pratt, *J. Chem. Phys.* **130**, 134306 (2009).

10. P.L. Ross and M.V. Johnston, *J. Phys. Chem.* **99**, 4078 (1995).

11. A. Miyoshi, N. Yamauchi, K. Kosaka, M. Koshi, and H. Matsui, *J. Phys. Chem. A*, **103**, 46 (1999).

12. X. Yang, J. Lin, Y.T. Lee, D.A. Blank, A.G. Suits, and A.M. Wodtke, *Rev. Sci. Instrum.* **68**, 3317 (1997).

13. D.R. Albert, D.L. Proctor, and H.F. Davis, *Rev. Sci. Instrum.* **84**, 063104 (2013).

14. S. G. Lias, "Ionization Energy Evaluation" in **NIST Chemistry WebBook, NIST Standard Reference Database Number 69**, Eds. P. J. Linstom and W. G. Mallard, Nation Institute of Standards and Technology, Gaithersburg MD, 20899, http://webbook.nist.gov, (retrieved June 27, 2016).

15. M.E. Corrales, V. Loriot, G. Balerdi, J. Conzalez-Vazquez, R. de Nalda, L. Banares, and A.H. Zewail, *Phys. Chem. Chem. Phys.* **16**, 8812 (2014).

16. T. Fleig and A.J. Sadlej, *Phys. Rev. A* **65**, 032506-1-8 (2002).

17. M. Ilias, V. Kello, T. Fleig, M. Urban, *Theor. Chem Acc.* **110**, 176 (2003).